# DESIGN AND INSTALLATION OF NOVEL SENSORS INTO THE CONTINUOUS CASTING MOLD

BY

MICHAEL KENNETH OKELMAN

THESIS

Submitted in partial fulfillment of the requirements
for the degree of Master of Science in Mechanical Science and Engineering
in the Graduate College of the
University of Illinois at Urbana-Champaign, 2008

Urbana, Illinois

Adviser:

Professor Brian G. Thomas

## Abstract

Microfabricated thin-film thermocouples (TFTCs) and Fiber Bragg Grating (FBG) sensors can be embedded in the nickel coating layer of a copper mold of a continuous caster to measure temperature and heat flux. Embedding sensors close to the surface has the advantage of sensitive real-time monitoring of critical thermal behavior without damping by the copper mold, as well as immunity to electromagnetic interference and resistance to hostile environments. The sensors require a robust attachment method that provides a secure bond between the sensor and the copper mold surface, has no air gaps, and is capable of surviving the acid pretreatment steps involved in the plating process in order to allow the sensor to be plated successfully before the copper mold can be put into service. A novel TFTC well suited for use in continuous casting molds has been designed and a method for embedding TFTCs in a coating layer was developed, as well as a computational model to quantify the effect of an air gap between the conductive sensor strip and the copper mold on heat transfer and stress in the coating layer. The signal output by FBG sensors embedded in a nickel coating layer has been investigated and can be predicted with simple equations. Furthermore, a method to successfully embed FBG sensors has been proposed based on the results of plating studies in this thesis and other literature.

## Acknowledgements

Funding for this work was provided by the National Science Foundation under contract CMMI 05-28668 and the UIUC Continuous Casting Consortium. Optical microscopy was carried out in the Frederick Seitz Materials Research Laboratory Central Facilities, University of Illinois, which is partially supported by the U.S. Department of Energy under grants DE-FG02-07ER46453 and DE-FG02-07ER46471. Special thanks to Mike Powers of Siemens VAI Services, LCC and Home Mojal of STAPLA Ultrasonics Corporation for their assistance.

**Table of Contents**

## 1. Introduction

Many of the problems in continuous casting arise during the initial solidification at the meniscus in the mold, including defects in the final cast product as well as cracks in the mold surface due to thermal stress. These problems dictate many aspects of steel quality and productivity. Although the mold hot face is an ideal location to monitor, it presents a very hostile environment, with copper mold surface temperatures from 200 to 400°C and instantaneous spikes that might reach 800°C during a mold level fluctuation. In current industrial practice, many thermocouples are inserted in continuous casting molds through drilled channels far from the hot face due to safety considerations. This limits their usefulness, as their response time is too slow to capture the rapid events that occur at the meniscus due to the dampening of the temperature signal caused by the thick copper mold between the solidifying steel and the thermocouple [1]. Sticker breakout detection systems, installed in many continuous casters worldwide, use thermocouple signals interpreted by control systems to take corrective action, but are limited by inadequate sensor technology and insufficient understanding of how to interpret the signals.

Microfabricated thin-film thermocouples (TFTCs) and Fiber Bragg Grating (FBG) sensors are capable of measuring temperature and heat flux within 1 mm of the meniscus by cost-effectively embedding them in the electroplated nickel coating layer used on many continuous casting molds. With the ability to place many sensors within close proximity of one another, embedded sensors are able to more accurately predict level fluctuations and quality problems, as well as providing additional insights into the casting process. Embedded sensors have the advantage of real-time monitoring at critical locations as well as immunity to electromagnetic interference and resistance to hostile environments.

This thesis highlights the design and installation process for a new type of mold sensor for use in the commercial continuous casting of steel. A novel TFTC capable of measuring temperature and heat flux has been designed for use in continuous casting molds. It has been demonstrated that wireless thermocouple technology can be used to transmit temperature data to a receiver in the caster pulpit. Numerous plating studies were performed to refine the sensor embedding process until a robust method was developed to embed TFTCs in a coating layer. A computational model was developed to quantify the effect of an air gap between the conductive sensor strip and the copper mold on heat transfer and stress in the coating layer. A thorough examination of the equations related to the signal output by FBG sensors embedded in a nickel coating layer and how the signal relates to temperature and strain has been conducted. Furthermore, a method to successfully embed FBG sensors has been proposed based on the results of plating studies in this thesis and other literature. The final goal is 1) to revolutionize online thermal monitoring of industrial continuous casting molds and 2) to create a new research tool to investigate meniscus behavior so that defect formation can be better understood.

## 2. Sensor Technology

### *2.1 Microfabricated Thin-Film Thermocouples*

Microfabricated thin-film thermocouples are desirable due to their small size and fast response. They have a temperature accuracy of +/- 2$^o$C and a 0.01s response time, capable of capturing temperature fluctuations of greater than 100$^o$C in 0.1s (much more sensitive than conventional thermocouples), and can be designed to measure heat flux as well as temperature. Thin-film thermocouples (TFTCs) are used in a broad range of applications for measuring surface temperatures [2-4].

The TFTCs considered here are fabricated on an insulating layer deposited on a nickel substrate. Standard Type K thermocouple materials (chromel and alumel) are used and covered with more insulating material. The selection of the insulating films is crucial to the survival and stability of the sensor, as this layer will isolate the sensor electrically from the underlying nickel substrate and from the final electroplated nickel embedding layer. The embedding layer protects the sensor from oxidation, chemical corrosion, wear, and contamination. The detailed process for sensor fabrication and embedding can be found elsewhere [5-7]. A schematic diagram illustrating the fabrication process is provided in Figure 1 [7]. These sensors are calibrated from ambient temperature to approximately 600$^o$C.

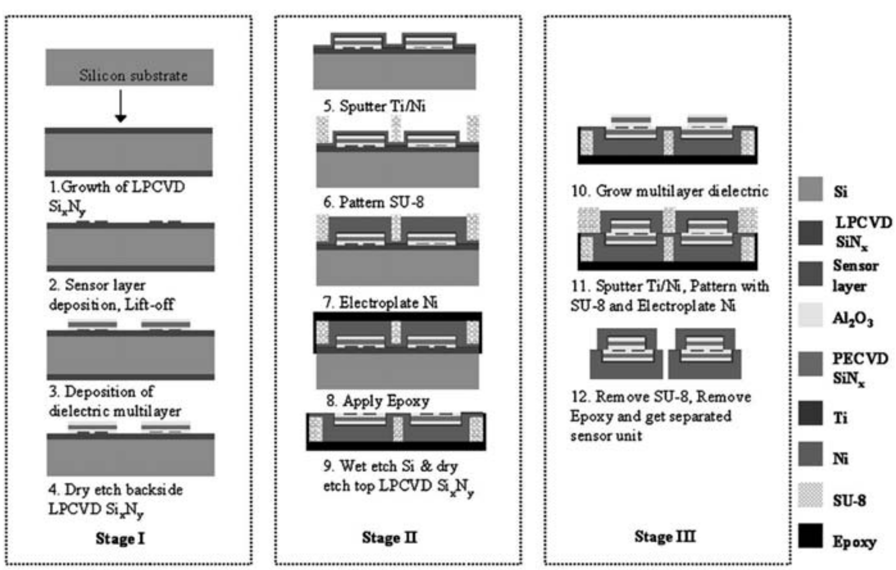


Figure 1. Schematic of fabrication of TFTC

*2.2 Fiber Bragg Grating Sensors*

Photosensitivity, a permanent change in refractive index or opacity induced by exposure to light radiation, was discovered at the Canadian Communications Research Center in 1978 by Ken Hill et al. [8] during experiments using germania-doped silica fiber and visible argon ion laser radiation. They discovered that when broad-band light is transmitted into the fiber core, the reflected light is of a single wavelength, called the Bragg wavelength. Since the core region has a higher refractive index, light is trapped in the core by total internal reflection, allowing light to travel large distances without varying much from the fabricated Bragg wavelength. Soon thereafter Butter and Hocker developed a fiber optics strain gauge based on measuring the change in optical path length of an optical fiber [9]. The work of Gerry Meltz et al. [10] allowed reflection gratings to be fabricated near 1550 nm, commonly used in the telecommunications industry.

The optical fiber is composed of a core region surrounded by a concentric cladding layer, usually made of silica. The diameter is 9 μm for the core of a single-mode fiber and 125 μm for the cladding. Often a plastic coating, such as the high-temperature resistant thermoset polyimide, is applied to outside of the fiber to reduce light loss caused by microbending and to provide handling protection to the delicate core and cladding (Figure 2). Polyimide coatings begin to degrade between 400 and 500°C [11].

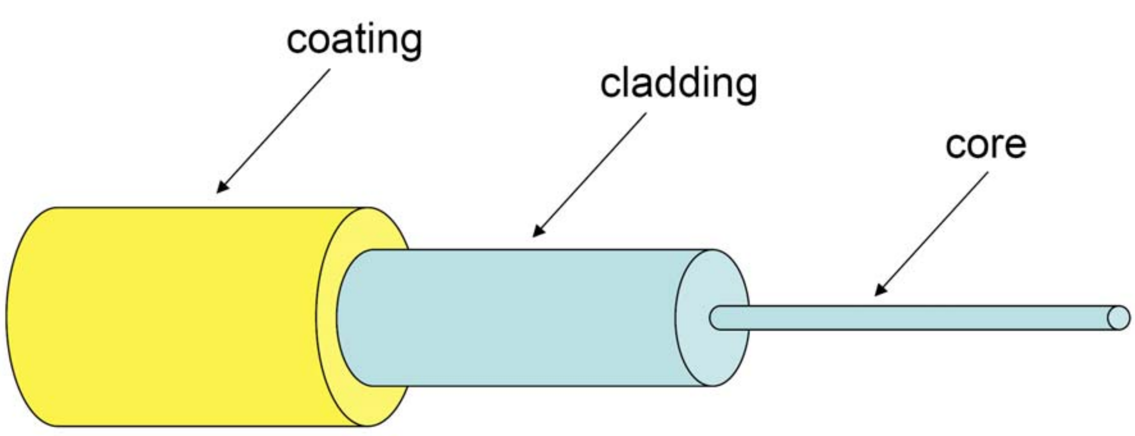


Figure 2. Illustration of the coating, cladding, and core of a coated fiber optic sensor (not to scale)

FBG sensors have recently been considered as promising candidates for integration into structural materials due to their immunity to electromagnetic interference, ease of embeddability, and resistance to hostile environments [11]. These sensors do not need electrical insulation, unlike TFTCs. FBG sensors can be used to measure temperature in the substrate in which they are embedded [11-14]. However, few papers demonstrate techniques for embedding FBG sensors in metal parts [14-18]. Tayler et al. and Lee et al. embedded a fiber Fabry-Perot Interferometer into aluminum by casting it in a graphite mold [15-17]. Baldini et al. embedded gold-coated optical fibers in titanium matrix composites produced by arc spraying [14]. X. Yu et al. embedded a FBG sensor into titanium by machining a shallow rectangular groove in the titanium alloy slice and coating it with a thin layer of epoxy [18]. None of these embedding techniques is feasible for embedding FBG sensors into the copper mold faces used in continuous casting of steel.

# 3. Embedding Sensors in the Electroplated Nickel Coating Layer

## *3. 1 Overview of Sensor Attachment Methods*

Before any research can be carried out to understand the behavior of embedded sensors, it is imperative that a robust manufacturing method be developed to embed sensors in the nickel coating layer of the continuous casting mold. Therefore, there is a crucial need to refine the embedding process through plating studies, as the sensor will be attached to the copper mold via the electroplating process used to apply the nickel coating layer. A successful attachment method must provide a secure bond between the sensor and the copper mold face, have no air gaps, survive the acid pretreatment steps, and allow the sensor to be plated successfully before the copper mold can be put into service.

Several methods exist to attach a sensor to a metal substrate including diffusion bonding [19-22], ultrasonic welding [23-25], and metallic paste [26, 27]. All of these methods allow dissimilar metals to be attached to one another. It is also possible to embed the sensor in a plating layer by plating around the sensor without it being first rigidly attached to the mold.

Diffusion bonding requires some solid solubility between the two metals to be joined, such as that between copper and nickel. The two metals must also survive the necessary temperature and pressure associated with the hot isostatic pressing (HIP) process. Ultrasonic welding is suitable for welding materials of different thicknesses, such as thin foils to thick substrates, and is less sensitive to surface contamination. Since it is a cold-phase friction welding technique, there is no melting. Electrically and thermally conductive silver paste (k = 109 W/m-K), used in adhesive and coating applications to 650°C, requires pressure, heat, and time to cure, but offers the same advantages as diffusion bonding and ultrasonic welding. Electroplating the attached sensor embeds it within the coating layer, which affords protection and a smooth exposed surface. This is very beneficial since the mold face must be flat. Voids can be catastrophic, leading to spalling of the coating layer, if it is subjected to sudden temperature changes [28, 29]. These methods are investigated in more detail in the following sections.

### *3.2 Attaching the Sensor Strip via "Hang and Plate" Method*

The electroplating method has the advantage of simplicity and low cost [30]. It also embeds the strip within the coating layer, which affords protection and a smooth exposed surface (after machining). This is very beneficial when the strip contains delicate sensors, or when the surface of the substrate and strip must be flat [5, 12]. However, when electroplating over complex geometries, defects such as voids or seams often appear, due to different rates of deposition throughout the geometry [31, 32]. Such voids can be catastrophic, leading to spalling of the coating layer, if it is subjected to sudden temperature changes [28, 29]. Previous electroplating studies include measurements of mechanical properties [33, 34] and models of the process [35-37]. Films of different surface morphology, thickness uniformity, grain size, and properties can be achieved by adjusting the current density, deposition technique, and/or composition of the solution bath [33]. Mathematical models of electroplating focus on the macro and micro-scale, including analytical models [35] as well as numerical models [36, 37] which are compared to experimental data. None of this previous work has quantified the effect of strip geometry on the formation of voids or seams during electroplating.

This work investigates the attachment of strips to a substrate by affixing the suspended strip above the substrate and electroplating in a commercial facility. Two plating trials comprised of four samples were performed to quantify the effect of strip width and gap thickness on the ability to attach thin strips to a copper substrate.

#### *3.2.1 Electroplating Process*

Commercial electroplating involves depositing a metal coating layer onto a metal substrate via electrolysis. The electroplating process requires an electric circuit be completed through the bath, which includes electrons flowing to the cathode (substrate) from the anode (source metal), as well as returning through a conducting electrolyte containing the metal ions, driven by a DC power source. For the nickel sulfamate plating bath used in this work, the reactions are:

Cathode: $Ni^{2+} + 2e^- \rightarrow Ni$; (1)

Anode: $Ni \rightarrow 2e^- + Ni^{2+}$ (2)

Metal ions arrive at the cathode surface through three principle paths: electrical migration, diffusion, and convection, both natural and forced, which replaces low ion concentration electrolyte with high ion concentration electrolyte [38]. Electrolyte fluid flow can be well represented by solving the incompressible Navier-Stokes equations in the entire bath, including the effects of thermal buoyancy. An additional time-dependent advection-diffusion equation is needed for the mass transport of the ions, which are carried by the liquid while diffusing through the liquid. The electric field, assumed to be steady-state, can be determined from a Laplace equation knowing the electric potential and the electrical conductivity. The effects of ion migration can be neglected if there is excess supporting electrolyte [36], such as the case for a large commercial bath.

It is also sometimes important to include time-dependent film resistance variation which occurs during the plating growth. The changing thickness leads to variations in the ion concentration and electric field near the cathode surface [36]. The theoretical plating thickness (assuming 100% current efficiency) can be calculated using Faraday's law [39, 40]:

$$T = \frac{ItM}{zF}\frac{1}{ad} \tag{3}$$

where $T$ is the thickness of the plating (cm), $I$ is the current (A), $t$ is the time (s), $M$ is the atomic weight (58.7 g/mol), $z$ is the ion valence (2), $F$ is Faraday's constant (96,500), $a$ is the substrate area ($cm^2$), and $d$ is the density of the plating material (8.9 $g/cm^3$). This equation holds both locally (if local values can be found), and on average (based on the total time and plating area).

### *3.2.2 Experimental Procedure*

Two plating trials comprised of four samples were performed. Samples 1 and 3 were placed on one copper substrate and samples 2 and 4 were placed on another copper substrate.

This arrangement made it possible to simultaneously investigate the effect of gap thickness and strip width on the ability to attach thin strips to a copper substrate.

In the constant gap thickness trial (samples 1 and 2), a thin triangular strip of rectangular cross section was held a constant distance above a copper substrate to test how the width of the strip affects the ability of nickel atoms to plate around the strip (Figure 3). For sample 1, the strip width ranged from 1623 to 4924 μm, while the gap thickness was kept constant at ~589 μm. For sample 2, the strip width ranged from 725 to 2759 μm, while the gap thickness was kept constant at ~1647 μm.

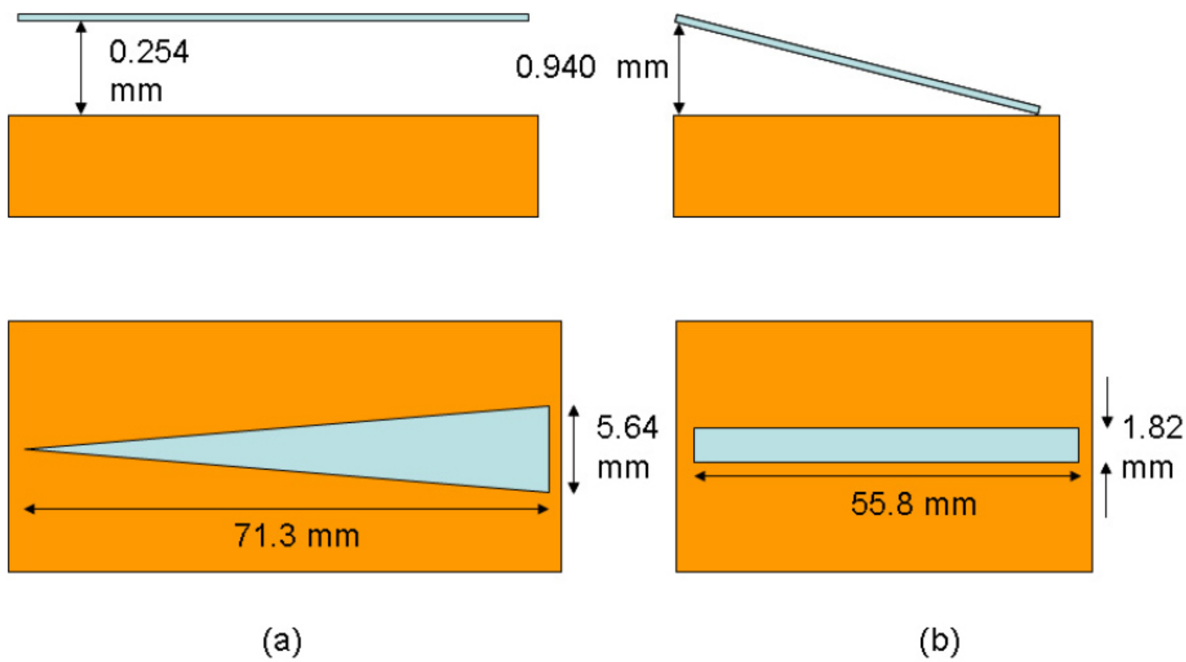


Figure 3. Illustration of (a) constant gap thickness trial (sample 1) and (b) constant strip width trial (sample 3)

In the constant strip width trial (samples 3 and 4), a rectangular strip of constant width was attached to the copper substrate a varying distance above the copper substrate to test how the distance between the nickel strip and the copper substrate, (i.e. the gap thickness), affects the plating ability, as seen in the above figure. For sample 3, the gap thickness ranged from 96 to 302 μm, while the strip width was kept constant at 1825 μm. For sample 4, the gap thickness ranged from 156 to 1317 μm, while the strip width was kept constant at 500 μm. Observed aspect ratios (strip width to gap thickness) ranged from 0.35 to 19.0.

The copper substrate was etched with nitric acid prior to the installation of the strips to clean the copper surface before electroplating. The nickel strips were cleaned by scrubbing with calcium carbonate and a 3-M burgundy Scotch-Brite$^{TM}$ abrasive pad. As shown in Figure 4, the strips were then suspended just above the copper substrate to perform a constant gap thickness trial and a constant strip width trial simultaneously. Yellow vinyl tape was attached to the copper substrate to achieve the desired gap thickness profile between the strips and the substrate. An investigation of the effect of electrically insulating the suspended strip from the grounded substrate was initiated by preventing some strips, via tape, from contacting the copper substrate. Each assembly was then masked prior to electroplating. In addition to protecting the edges, the masking included attaching both insulating and conducting pieces to the cathode to encourage uniform current density and plating thickness. Each assembly was pretreated by rinsing with DI water and immersing in a 10% sulfamic solution to clean the surfaces. The strips did not seem to suffer any negative effects due to this pre-treatment. Each assembly was then placed in a nickel sulfamate bath with a concentration of 1.5 mole/L at a commercial plating facility in Benton Harbor, Michigan. Due to the high solubility of the salts of sulfamic acid, high concentrations of nickel ions are possible, permitting high rates of plating. This same commercial facility and procedure is used to plate copper continuous casting molds for the steel industry.

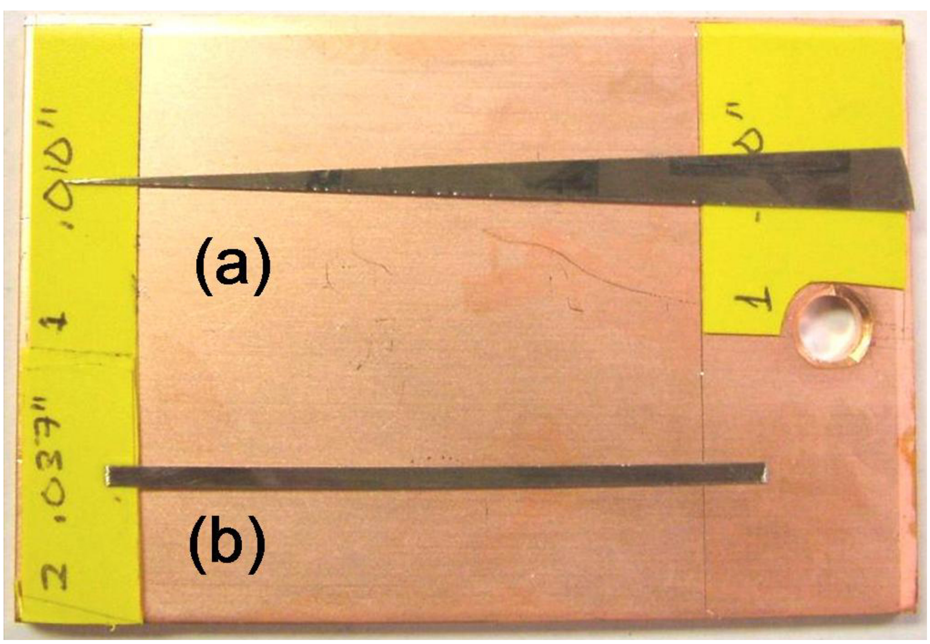

Figure 4. Nickel strips mounted to the copper substrate (a) sample 1 (b) sample 3

The substrate area was 2500 $mm^2$; so 0.75 amps of current were required for 0.0254 mm of plating per hour.  A potential of 1.8 volts was applied between the copper substrate and suspended nickel strips (cathode) and a grated metal basket of nickel pieces that comprised the anode located ~150mm away in the bath.  After 65 hours a total of 2.08 mm of nickel (ultrasonic measurement) was deposited on the copper substrate.

For the constant gap thickness trial and constant strip width trial the electroplated nickel strip was cut into cross-sections using wire electrical discharge machining (EDM). Each sample was mounted in epoxy, rough ground with 180 grit SiC paper, hand ground with 240, 320, 400, and 600 grit, and machine ground using 800 and 1200 grit.  Machine polishing was also performed with a short knap cloth and 1 μm solution and 0.3 μm solution when necessary to obtain a mirror-like finish.  Etching was performed by immersing each sample in 1 part nitric acid, 1 part acetic acid (glacial), and 1 part DI water for 15 seconds.

### *3.2.3 Results and Discussion*

The typical structure of the plating layer relative to the strip location and void that formed beneath it is shown in Figure 5.  Optical microscopy was used to identify the strip location and the surrounding plating structure.  The void thickness and width were measured from traces of the photographs.  In addition, the gap thickness and the thickness of the nickel plating under the strip were measured at 6 different locations:  above and below the void at left, right, and center (Figure 6).  For both trials, a plot of the void thickness, void width, gap thickness, and strip width versus the distance along the copper substrate was created (Figure 7).

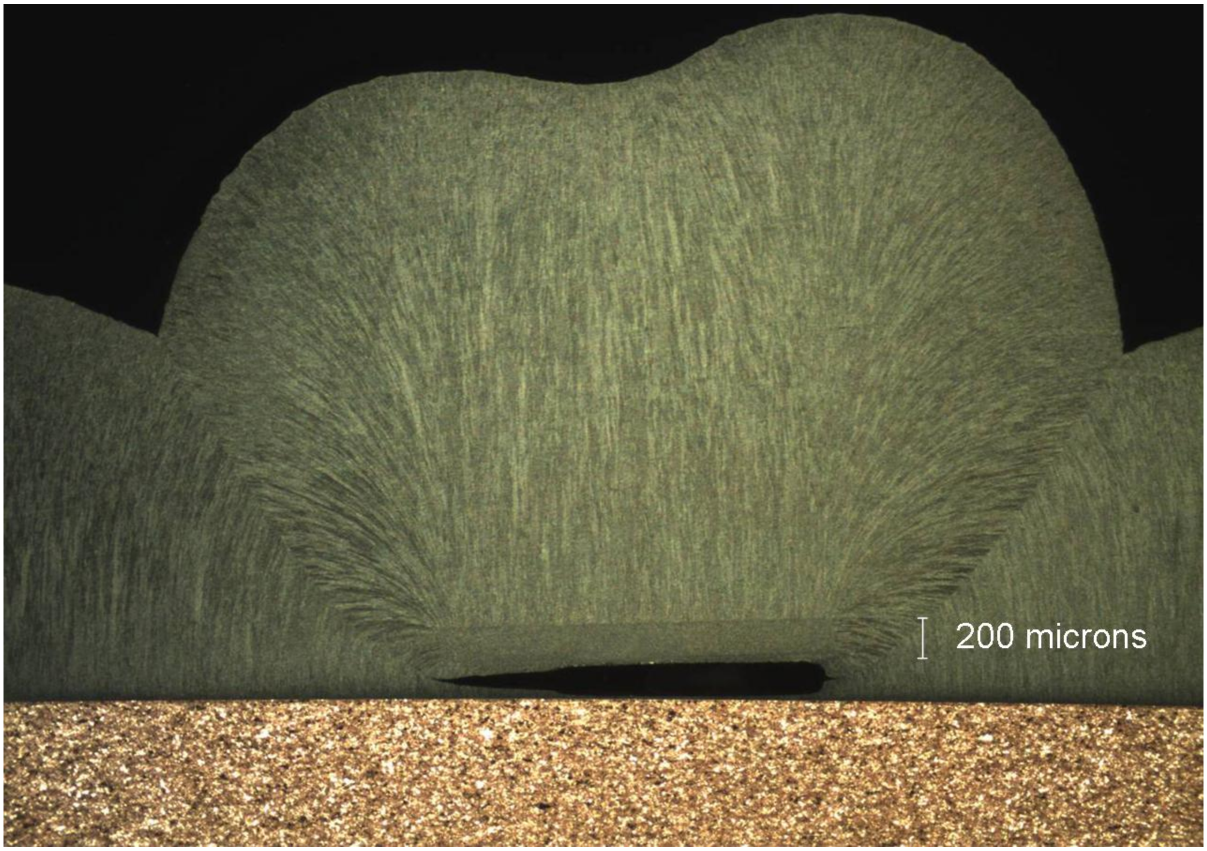

Figure 5. Optical microscope photograph of cross section of nickel plated copper substrate with nickel strip showing seams between impinged plating layers, nickel strip, and void

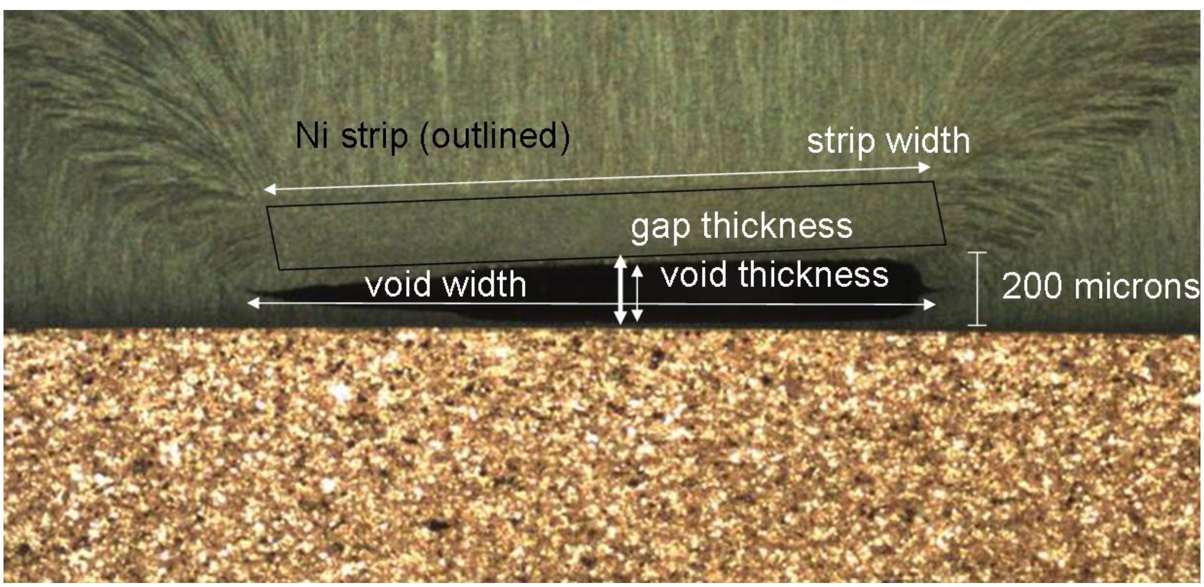

Figure 6. Close-up of void region where quantitative measurements were made

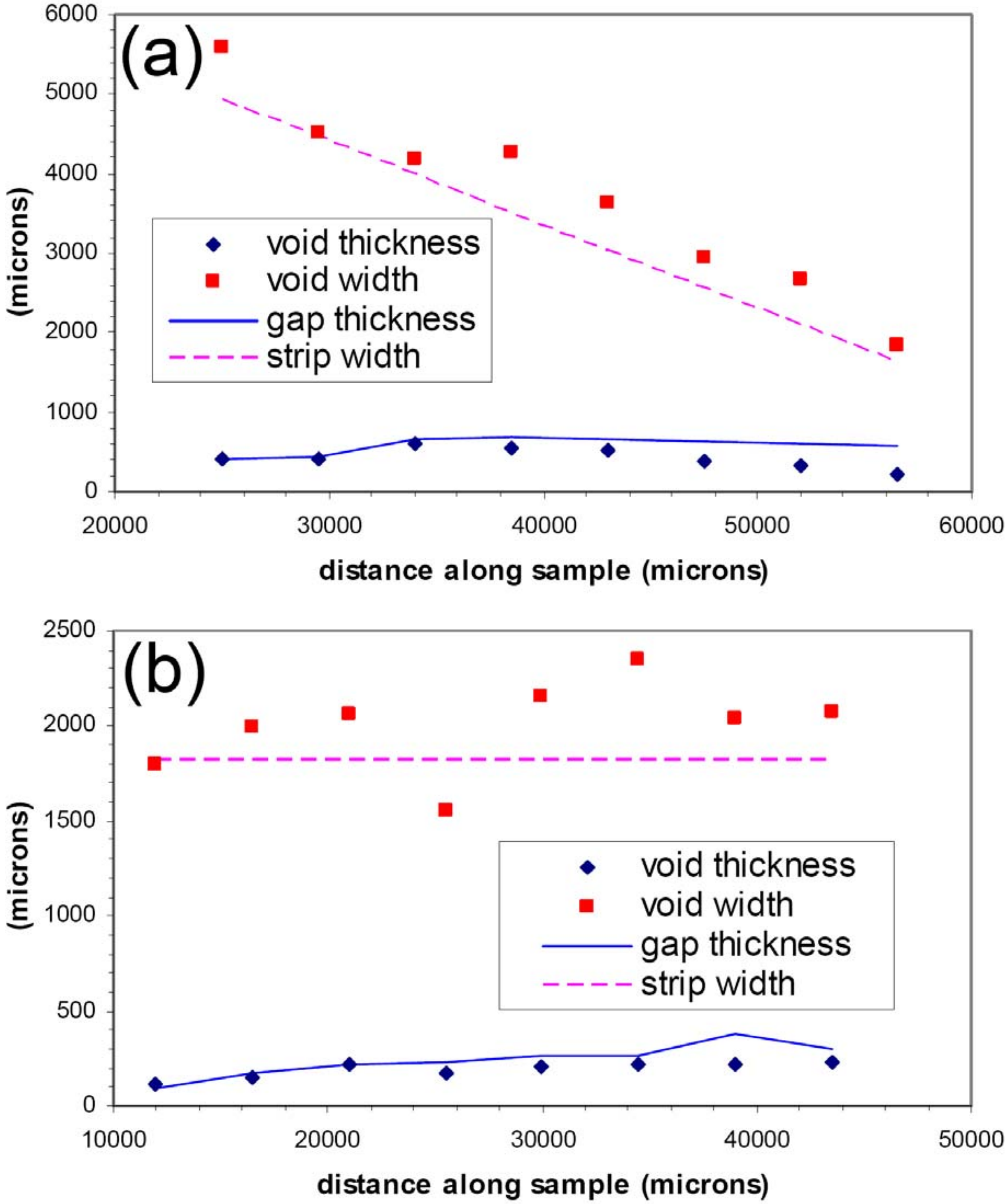


Figure 7. Impingement often occurs just past the edge of the strip which causes the void width to be greater than the strip width and form seams at the edge of the void (a) sample 1 (b) sample 3

Plating growth impingement often occurs just past the edge of the strip which causes the void width to be greater than the strip width and form seams at the edge of the void. The above figure also shows that as the strip width decreases, the void thickness decreases and more plating occurs under the nickel strip. Based on this observation, it is proposed that the extent of plating under the nickel strip is related to the aspect ratio, defined as the ratio of the strip width to the gap thickness (Figure 8). Specifically, more plating reaches under the nickel strip as the aspect ratio decreases. In the constant gap thickness trial, this is due to the decrease in strip width, while in the constant strip width trial the same observation is due to the increase in gap thickness.

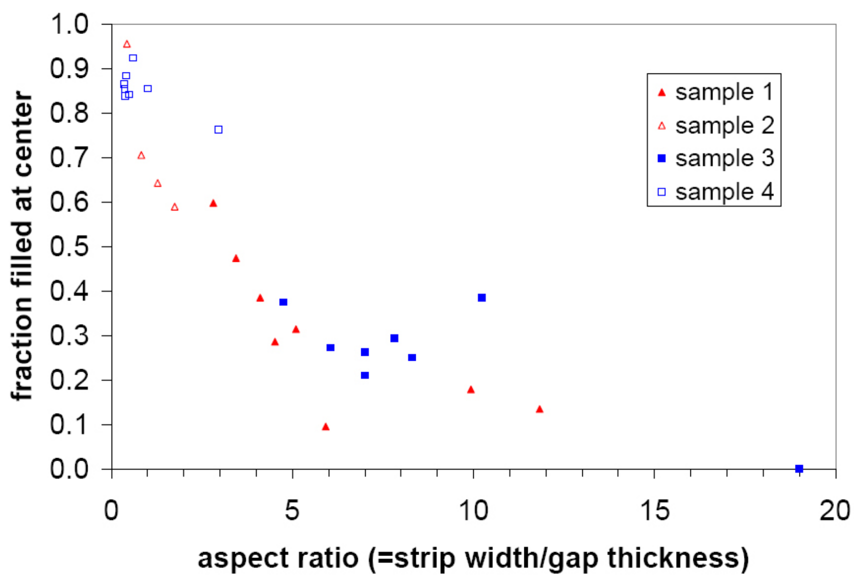

Figure 8. More plating is obtained underneath the strip as the aspect ratio decreases

The sequence of events leading to the observed microstructure and void shape is sketched in Figure 9. Nickel plated onto the copper substrate and to the top, bottom, and sides of the nickel strip, even when there was no physical connection to the copper substrate. The plating layers on each of the nickel strips grew outwards at the same rate regardless of whether or not it was insulated on its ends. This indicates that the nickel strip is effectively grounded through the conductive bath across the short distance to the copper substrate. The theoretical average deposit thickness was calculated as 2.40 mm (Eqn. 3) which is close to the 2.08 mm measured. Minor plating thickness abnormalities at the edges of the small copper substrate were responsible for the difference.

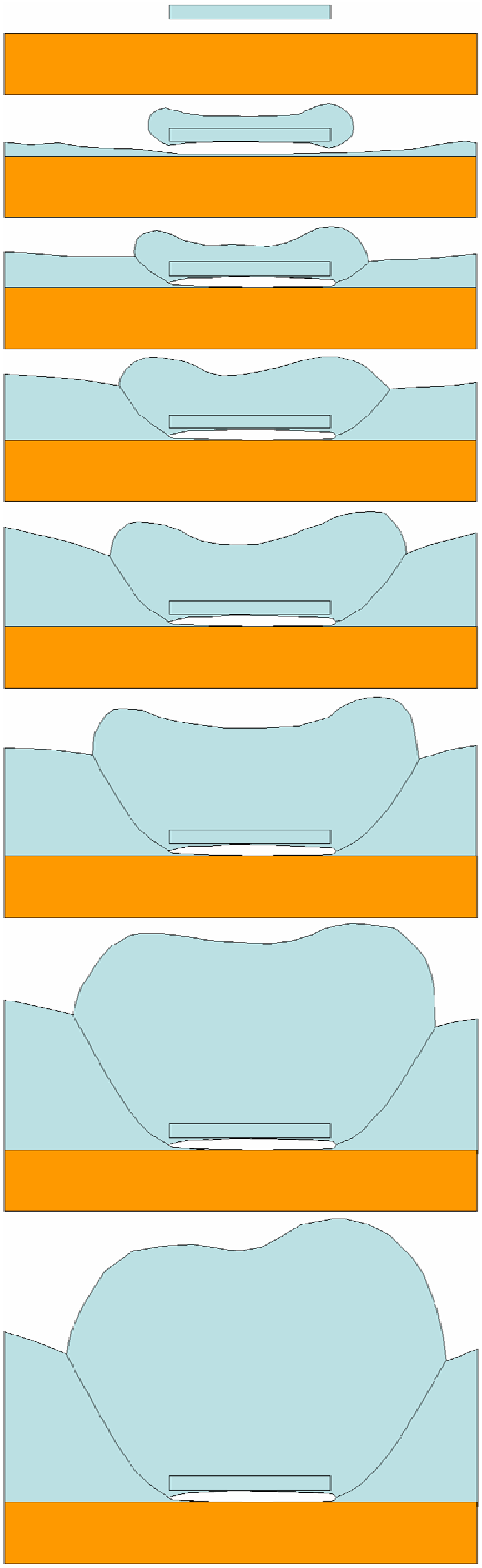

Figure 9. Early on the plating growing from the corners of the strip contacts the plating originating from the substrate and “starves” the region beneath the strip from nickel ions, creating a void

The plating depositing onto the nickel strip corners is faster than elsewhere, owing to the higher local current density. Thus, it quickly grows to contact the plating layer originating from the copper substrate. This traps a region of electrolyte beneath the strip. This region becomes "starved" of nickel ions because the transport of ions is prevented (i.e. migration and diffusion), owing to its isolation from the rest of the bath, as convection is unable to replace the low ion concentration electrolyte with high ion concentration electrolyte. Even moving the strip almost three widths away from the substrate is not enough to prevent void formation (Figure 10). As in shrinkage-cavity macroporosity observed in metal foundry castings [41-43], a liquid region completely surrounded by solid will result in a void, as seen in the figure. As a consequence, every rectangular specimen contained a void between the rectangular strip and substrate.

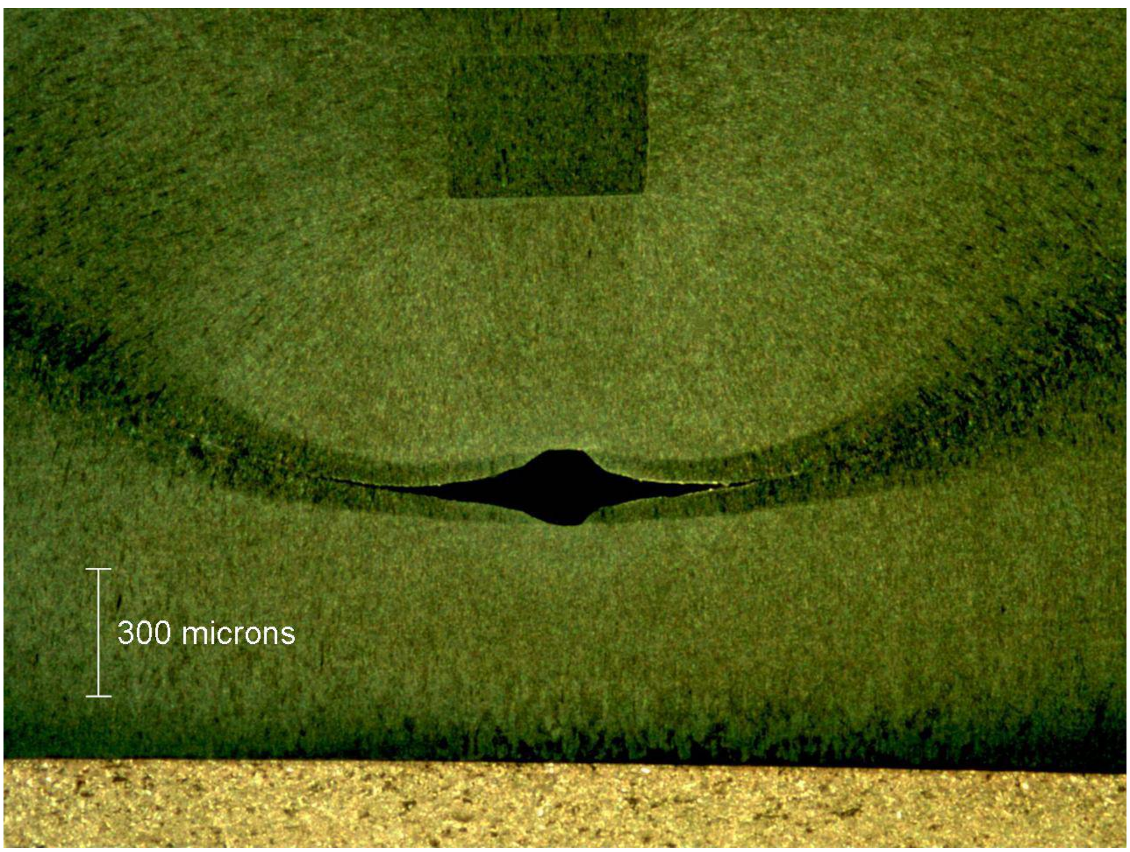


Figure 10. Even for small aspect ratios the geometry of the strip causes the plating growths to contact in a way which produces seams and a void

### 3.2.4 Conclusions on "Hang and Plate" Method

Two plating trials comprised of four samples were performed to evaluate the plating ability to attach thin strips to a copper substrate by measuring the occurrence and size of voids found under the strips. As the strip width decreases, or gap thickness increases, more plating penetrates under the strip. In other words, the aspect ratio roughly governs the fraction of the gap filled by the plating. Voids form beneath rectangular strips even for aspect ratios less than one. The plating growing from the strip corners contacts the plating originating from the substrate and “starves” the region beneath the strip from ions. The results of this study can be used to minimize or avoid void formation in commercial electroplating of suspended strips which is of great importance in the installation of sensor strips in the coating layer of continuous casting molds.

## 3.3 Ultrasonically Welding the Sensor Strip to the Copper Mold

An ultrasonic welding trial was performed at the STAPLA Ultrasonics Corporation laboratory in Wilmington, MA to determine the feasibility of attaching a nickel strip and a TFTC to a copper substrate. The 4 mm wide nickel strip was approximately 0.421 mm thick and the copper substrate was approximately 3 mm thick. The bond was achieved using a Condor Universal Weld Head. Neither the nickel strip, TFTC, nor copper substrate was cleaned prior to the test, due to the ability of ultrasonic welding to breakup oxide/contaminant layers. After attachment via ultrasonic welding, the assembly could be nickel plated.

Ultrasonic welding has not been found to be an acceptable solution to the sensor attachment problem. Although the ultrasonic welding equipment is able to attach the two dissimilar metals, Figure 11 shows that more than one weld can distort and crack the TFTC. The large gaps observed between the sensor and the substrate would likely not be filled in during the electroplating process (see previous section). According to the ultrasonic welding equipment manufacturer, past experiences have indicated that ultrasonic welding near, around, or on top of sensors has lead to irreversible damage. Furthermore, the machining pattern caused by the weld horn is unavoidable. Thus, this method is not recommended for sensor attachment.

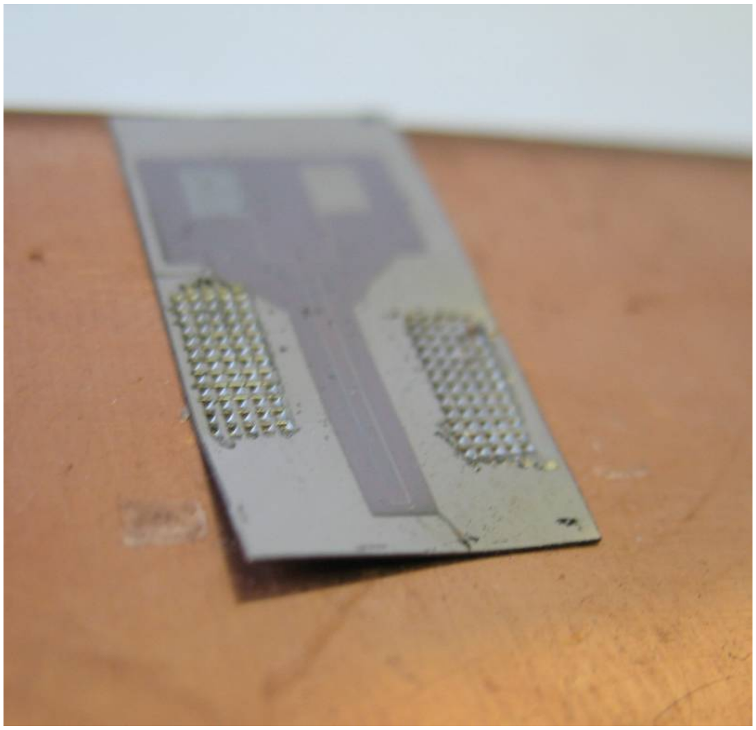
Figure 11. Ultrasonic welding caused the TFTC to distort and crack

*3.4 Using Silver Paste to Attach the Sensor Strip to the Copper Mold*

Pyro-Duct™ 597A electrically and thermally conductive silver paste (k = 109 W/m-K), an inorganic system for adhesive and coating applications up to 650°C, was purchased from Aremco Products, Inc. A nickel strip 4 mm wide and approximately 0.411 mm thick was chosen for the silver paste trial. Both the nickel strip and copper substrate were cleaned with alcohol to remove any grease or debris. An area the size of the nickel strip was masked off on the copper substrate with black vinyl tape, and followed by the application of a layer of reinforced fiberglass tape to assist in silver paste removal. A section of clear packing tape was attached to the top face of the nickel strip to prevent any silver paste from adhering. A thin layer of silver paste approximately 0.25 mm thick was then applied to the masked copper substrate. The nickel strip was then pressed into place. An image of the masked copper substrate, with clear packing tape removed, can be seen in Figure 12. In order to cure the silver paste, pressure was applied for two hours and the tape was removed and all unwanted paste was discarded. The cure was completed by placing the nickel strip and copper substrate in a 100°C oven for two hours.

Figure 12. The masked copper substrate showing the silver pasted nickel strip prior to oven curing

After curing the silver pasted nickel strip and copper substrate was sent to the plating facility in Benton Harbor, MI. The copper substrate was etched with nitric acid to clean the copper substrate before electroplating. The assembly was then masked to prepare for electroplating. In addition to protecting the edges, the masking included attaching insulating pieces to encourage uniform current density and plating thickness. The assembly was pretreated by rinsing with DI water and immersing in a 10% sulfamic solution. The nickel strip and silver paste did not seem to suffer any negative effects due to this pre-treatment. The assembly was then placed in a nickel sulfamate bath overnight.

The electroplated nickel strip was cut into cross-sections using wire electrical discharge machining (EDM). Each sample was ground, polished, and etched. Etching was performed by immersing each sample in 1 part nitric acid, 1 part acetic acid (glacial), and 1 part DI water for 15 seconds.

As Figure 13 demonstrates, a sensor strip can be attached to a copper substrate via conductive silver paste and successfully plated over without any air gaps. The nickel plating completely covers the silver paste without any abnormalities. Thus, this process is a suitable method to embed a TFTC sensor into the mold coating layer. However, the time and skill involved in this process is considerable.

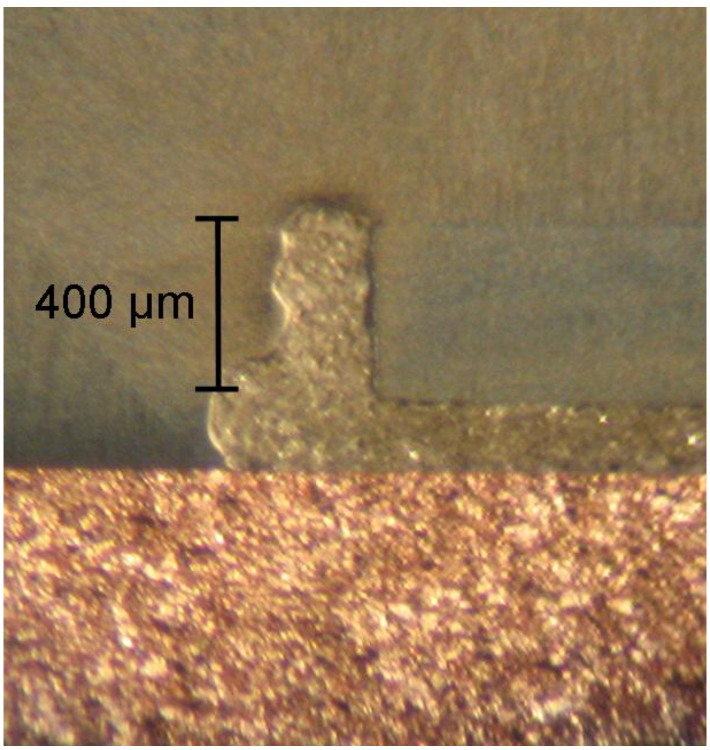

Figure 13. Close up view of silver pasted nickel strip

### *3.5 Embedding Non-conductive FBG Sensors via Electroplating*

An additional two plating studies were performed to investigate the effect of strip shape (rectangular versus circular) and strip conductivity (non-conductive versus conductive) on the ability to attach thin strips to a copper substrate. Sample 5 consisted of a cylindrical "strip" of non-conducting optical fiber suspended 0 to 1524 μm above a copper substrate.

The optical fiber was composed of a plastic protective outer coating surrounding a cladding layer and glass inner core. With the plastic coating the fiber has a diameter of 200 µm, while the cladding layer surrounding the glass core has a diameter of 125 µm. The glass core itself is only 9 µm in diameter. Sample 6 consisted of a cylindrical tube of 316 stainless steel with an outer diameter of 254 µm and inner diameter of 127 µm suspended a constant distance of about 10 µm above a copper substrate. Both samples were placed on separate substrates.

The optical fiber (sample 5) and the stainless steel tube (sample 6) were not treated before attachment to the copper substrates. However, prior to plating each assembly (sample and substrate) was pretreated by rinsing with DI water and immersing in a 10% sulfamic solution to clean the surfaces. The strips did not seem to suffer any negative effects due to this pre-treatment. Each assembly was then placed in a nickel sulfamate bath at the same commercial plating facility in Benton Harbor, Michigan for plating. After plating, several samples were ground, polished, and etched following a similar procedure as outlined above. Again, etching was performed by immersing each sample in 1 part nitric acid, 1 part acetic acid (glacial), and 1 part DI water for approximately 15 seconds.

When plating over a non-conductive cylinder (sample 5), complete filling is observed, as seen in Figure 14 and Figure 15. The lack of a void in this geometry is expected because 1) without corners, the growth rates from the cylinder surface are almost uniform, and 2) the plating growing from the copper substrate has further distance to reach the cylinder extremities. The figure shows that the nickel grain structure originated from the copper substrate and grew up and around the non-conductive cylinder. The cylinder remained non-conductive and uncharged so no detectable deposit formed on its surface. In the case of a conductive cylinder (sample 6), the plating layer growing from the cylinder is almost uniform, owing to the lack of corners. Thus, the plating from the copper substrate first contacts the cylinder near its center. This avoids entrapping electrolyte and therefore prevents void formation. Thus, cylindrical fibers experience sound plating, regardless of their insulating properties. Due to their small size, optical fiber sensors also have the advantage of being plated in "clusters" to achieve high spatial resolution, as seen in Figure 16.

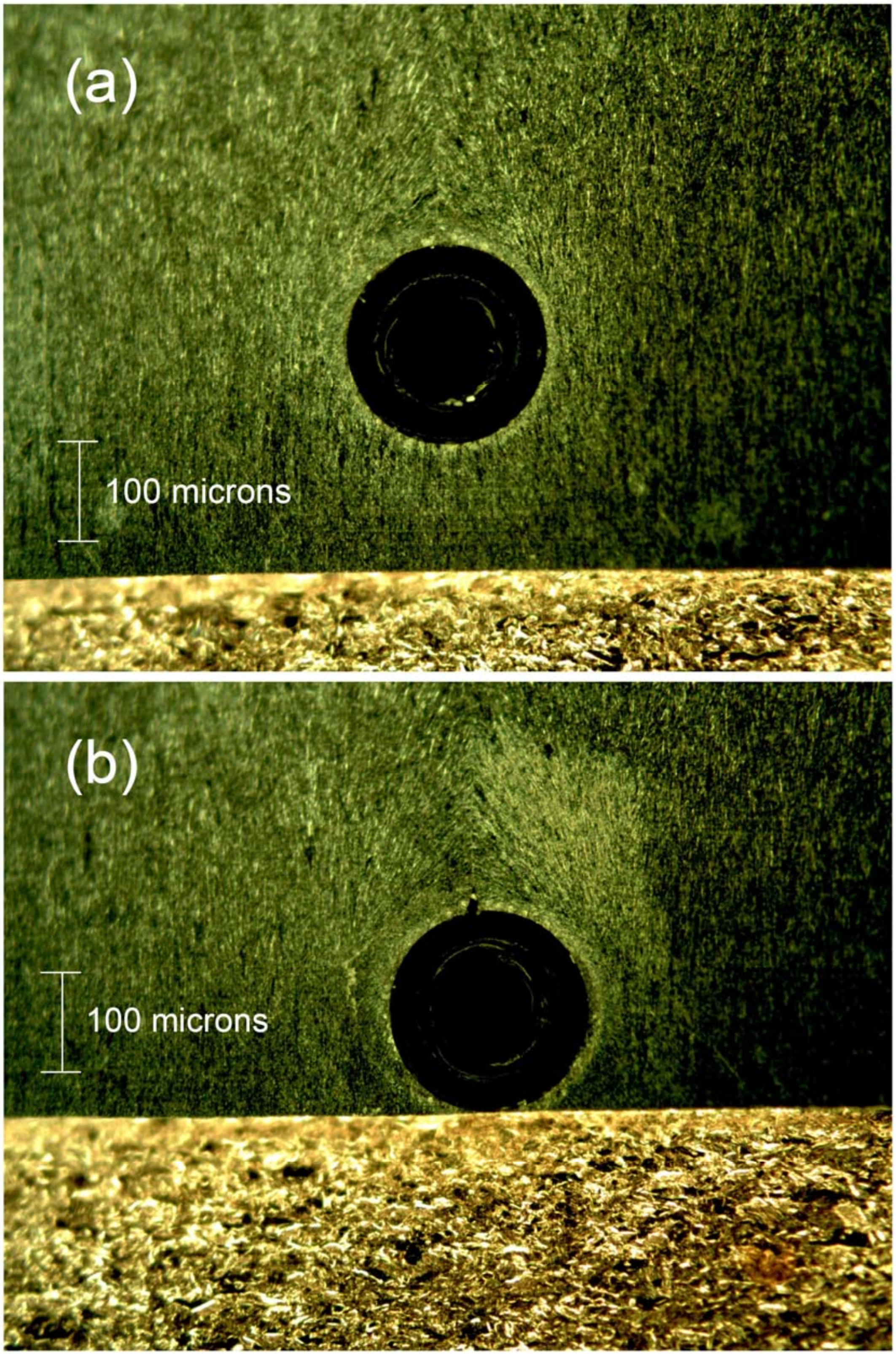


Figure 14. Optical microscope photograph of cross-section of nickel plated copper substrate with non-conductive cylinder (sample 5) (a) cylinder near substrate and (b) cylinder contacting substrate (200 µm diameter, plastic coated optical fiber)

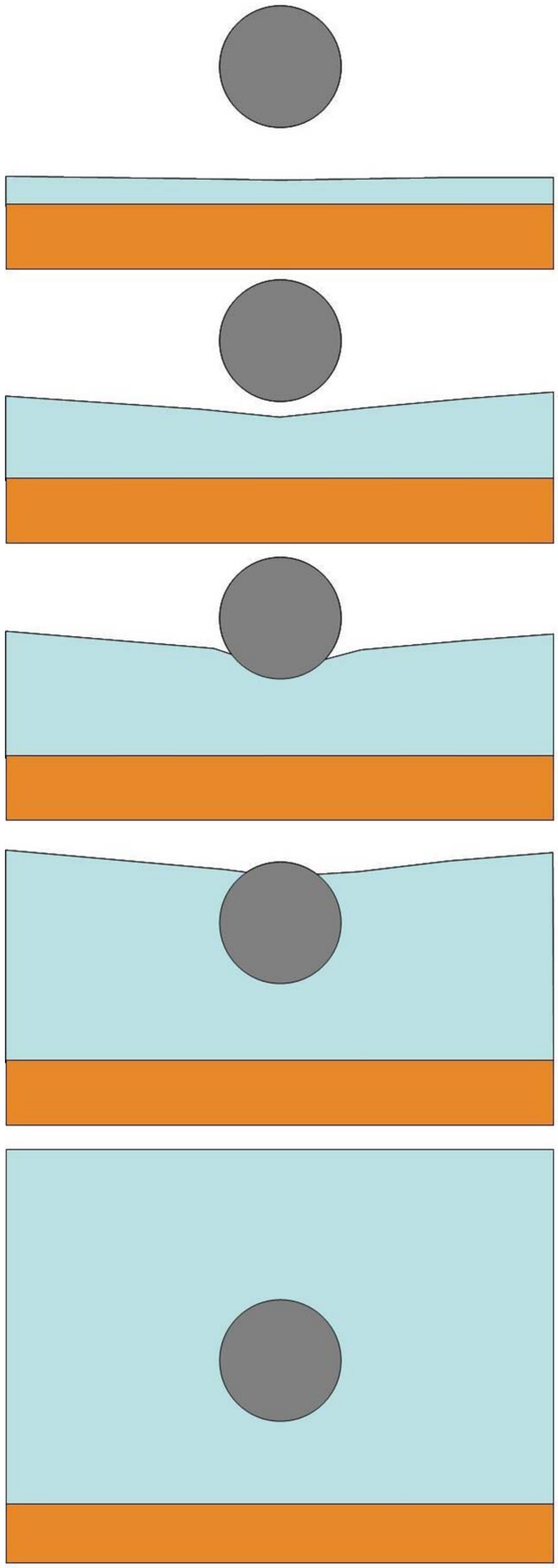

Figure 15. Complete filling is observed when plating over a non-conductive cylinder as the plating growing from the substrate does not contact the cylinder in a way which produces a trapped liquid region

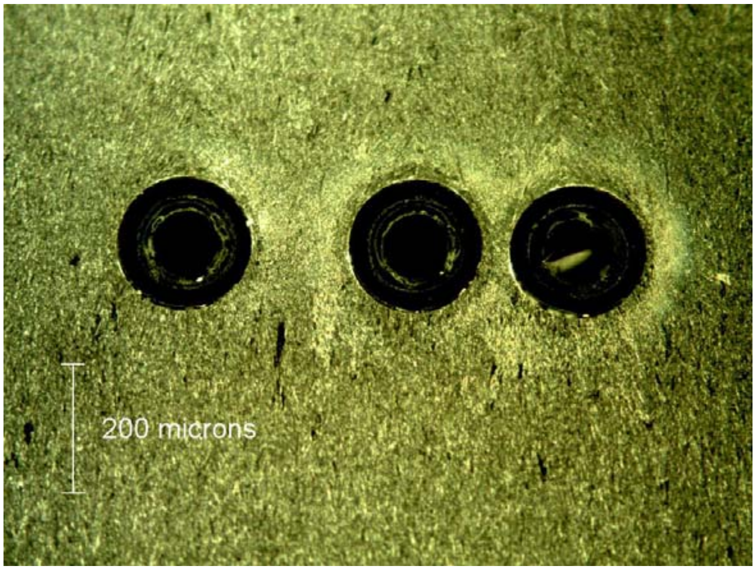


Figure 16. FBG sensors can be plated in "clusters" to achieve high spatial resolution (200 μm diameter, plastic coated optical fiber)

Once it was demonstrated that cylindrical fibers experience sound plating, regardless of their insulating properties, a reflection-type FBG sensor of Bragg center wavelength ($\lambda_{CW}$) 1542.80 nm and transmission-type FBG sensor of center wavelength 1543.30 nm (both purchased from O/E Land Inc.) were nickel plated onto a copper substrate following a similar procedure as outlined above. The polyimide coating on the sensors gives them an overall diameter of 155 μm, enabling them to easily fit within the 300 μm to 400 μm thick nickel coating layer used on molds. Although the two FBG sensors were successfully nickel plated onto a copper substrate (Figure 17), the reflection-type sensor was damaged in handling. The fragility of the sensors is a major issue that must be addressed before FBG sensors can be used in the copper molds of the commercial continuous casting process.

Figure 17. FBG sensors can be successfully nickel plated

## 4. Sensor Design and Installation

### *4.1 Microfabricated Thin-Film Thermocouples*

A preliminary design for sensor installation into the narrow face of a continuous casting mold is illustrated in Figure 18. As the "hang and plate" method of attaching the TFTC proved that an air gap free bond was not possible and ultrasonic welding destroyed the fragile sensor, the silver paste method has been proposed as the solution, despite the time and skill necessary to attach the TFTC prior to plating, as this method lends itself to a secure bond between the sensor and the copper mold face without air gaps. The silver paste plating studies have also showed that this method is capable of surviving the acid pretreatment steps and allows the sensor to be plated successfully.

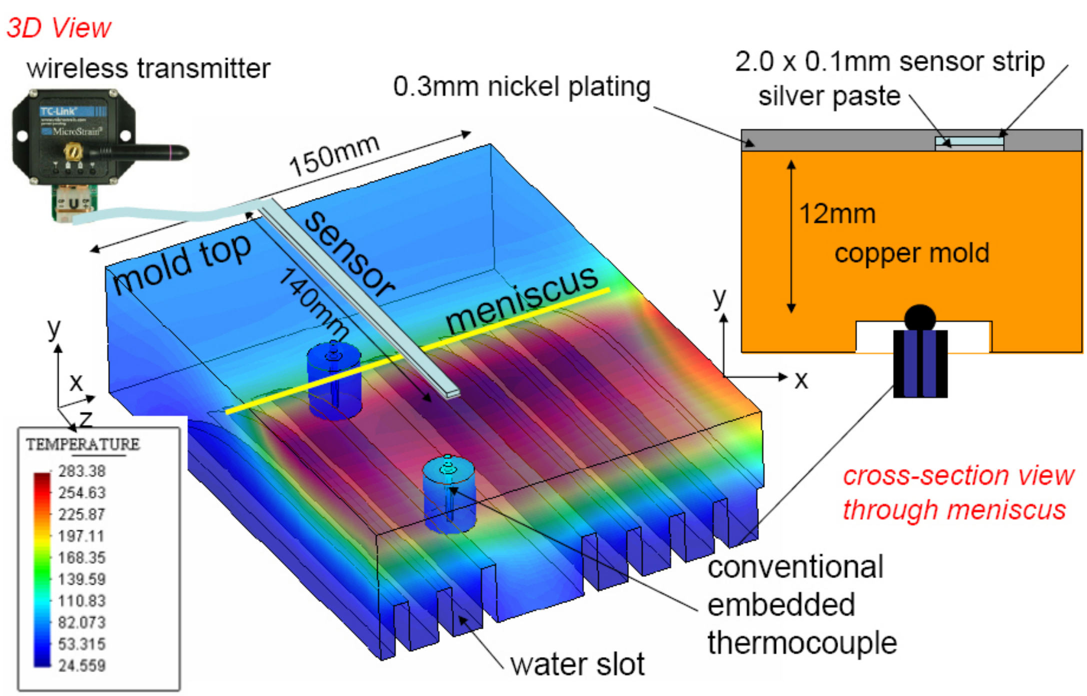

Figure 18. Proposed placement of sensor into nickel coating layer of continuous casting mold (temperature in Celsius)

Minor cosmetic changes to the copper mold hardware are necessary to accommodate the presence of a novel sensor system. The sensor pad containing the wire junction points will protrude out of the top of the narrow face copper mold and nickel plating, thereby making wire connections possible after plating. The sensor pad and wire connections will be shielded from the hostile environment encountered at the top of the copper mold by liberally applied silicone and a modified, recessed narrow face top cap. The wires will be run a short distance to a wireless transmitter which will transmit the temperature and/or heat flux signal to the control-room operator display or other computer. The wireless system supports simultaneous data transmission from multiple sensors, theoretically allowing thousands of sensors to be installed into a mold.

TFTCs can be designed to measure temperature, heat flux, or both [44]. Temperature differences can be measured across two locations separated by two layers of ceramic of different thicknesses, according to Figure 19, in order to measure heat flux using the equation:

$$q'' = k\frac{T_1 - T_2}{x_1 - x_2} \tag{4}$$

where $k$ is the coefficient of thermal conductivity of the ceramic, $T_1$ - $T_2$ is the temperature difference across the two layers of ceramic, and $x_1$ and $x_2$ are the thicknesses of the two ceramic layers [44, 45]. The signal output can be increased by connecting pairs of thermocouples in series to form a thermopile. This setup is capable of accurately measuring both steady and transient heat fluxes and provides good sensitivity due to the large output signal [46, 47].

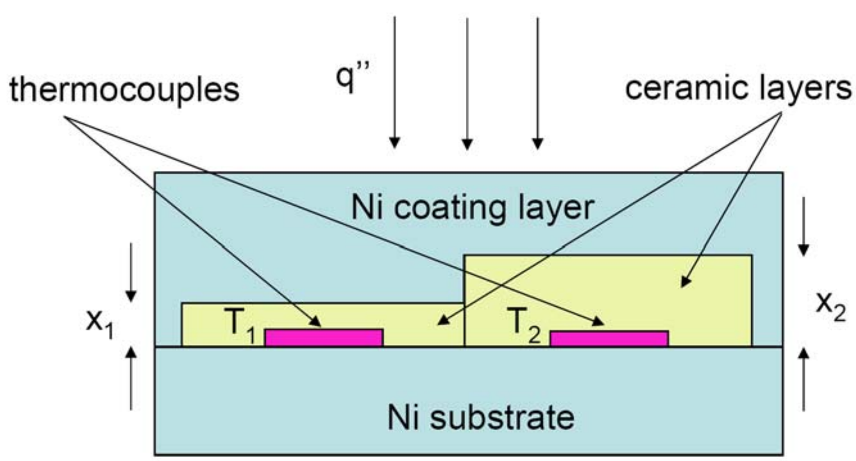


Figure 19. Heat flux can be measured by a thermopile with two layers of ceramic

A novel TFTC that can measure both temperature and heat flux (using thermopiles) for use in a continuous casting mold has been designed (Figure 20). The four thermopiles are necessary for high spatial resolution of the thermal events in the meniscus region of the mold. In addition to a thermopile (shown with nickel coating layer removed for detail), each of the four sensor arrays contains a separate Type K thermocouple (chromel-alumel) for temperature measurement only. The leads of each of the four thermopiles and thermocouples are connected to the sensor pad which protrudes from the top of the copper mold.

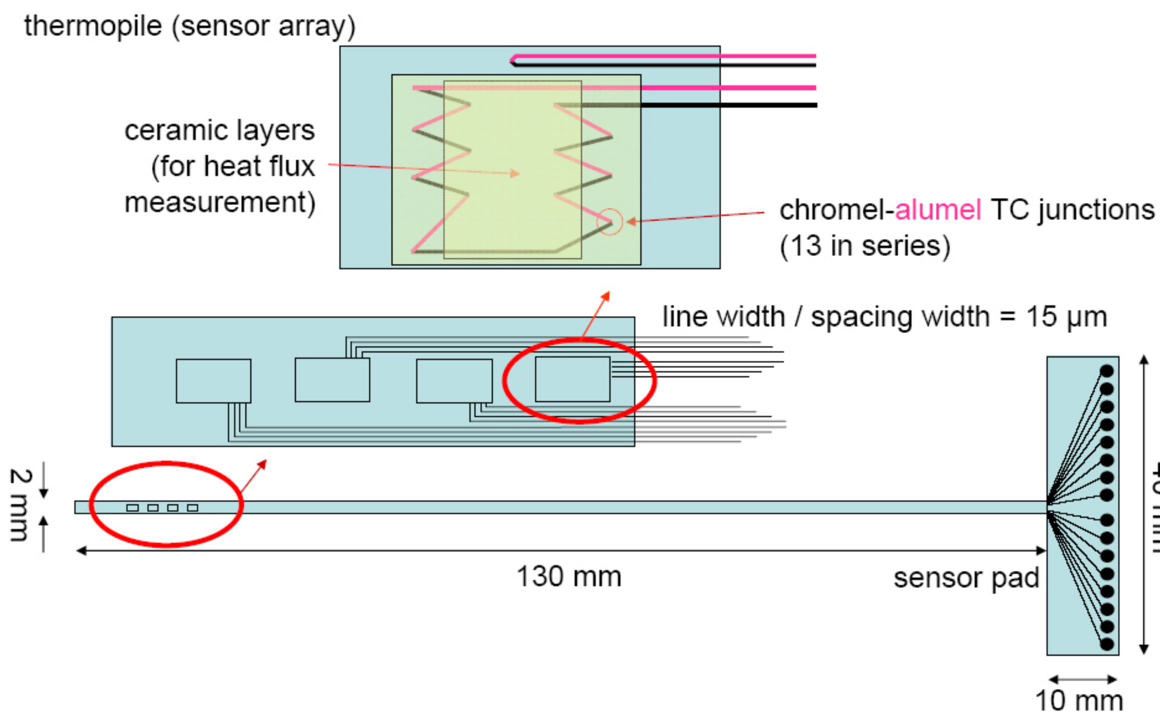


Figure 20. TFTC designed for use in a continuous casting mold

A wireless thermocouple system that is compatible with the TFTC sensor was obtained from MicroStrain®. The wireless system was tested in the presence of an electromagnetic field (provided by an electromagnetic brake, or EMBr) at a commercial steel mill in Riverdale, IL. The transmitter was attached to a Type K thermocouple which was submerged in room temperature water. A thermometer was used to validate the accuracy of the thermocouple measurement. The receiver was placed in the caster pulpit approximately 20 meters away and attached to a laptop. During the measurements, the position of the transmitter and the current of the EMBr were varied. At all times the wireless system was shown to maintain communication between the transmitter and receiver and provide an accurate temperature measurement (Figure 21).

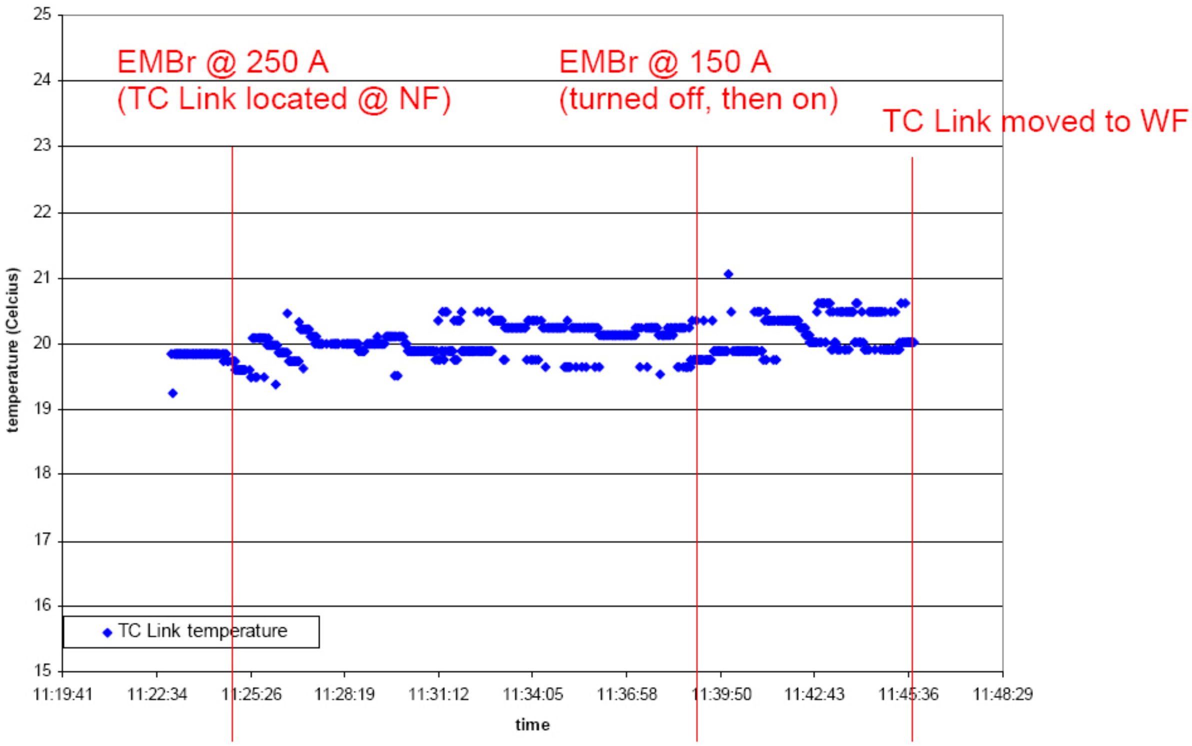


Figure 21. The wireless system maintained communication and provided an accurate temperature measurement for the duration of the test (NF=narrow face, WF=wide face)

### *4.2 Fiber Bragg Grating Sensors*

Technically, FBG sensors do not measure temperature or strain. The interactions between the sensor and substrate are complex, so interpretation of the sensor signals is not simple. It would be more accurate to say that FBG sensors measure Bragg wavelength shifts from which temperature and strain can be determined. Specifically, the signal output by a FBG sensor is a combination of at least four quantities (three principle strains and temperature) [48]. It is possible to calibrate a FBG sensor (or FBG sensor system containing more than one sensor) for a given load, but the results would only be valid under conditions that produce a nearly identical temperature and strain as those used during calibration. Instead, for structurally embedded FBG sensor temperature measurement systems it is better to determine the optical properties of the FBG sensor as a function of temperature and wavelength [48] and use them together with the FBG sensor's strain-based properties to predict the temperature.

The signal output by the FBG sensor corresponds to the temperature and strain *at* the FBG sensor, not to the substrate, as a sensor embedded inside the substrate disturbs the strain and temperature field. The signal output by the FBG sensor (the "temperature" and "strain" at the sensor) must be related to the temperature and strain in the host material. This analysis has been conducted for both bare [49] and coated fiber optic sensors [50, 51]. The results show that some of the strain components inside the sensor may differ if the sensor is bare or coated. Furthermore, the difference depends on the thickness and properties of the coating.

As inferred from above, when a strain is applied to a FBG sensor its grating spectral response, or Bragg wavelength, is changed (i.e. the Bragg wavelength is dependent on both temperature and strain). Assuming that the bond between the fiber and the substrate is strong (i.e. the "temperature" and "strain" at the sensor is equal to the temperature and strain of the substrate), the total Bragg wavelength shift for an embedded FBG sensor has two components:

$$\Delta\lambda_{total} = \Delta\lambda_{temperature} + \Delta\lambda_{strain} \tag{5}$$

The thermal effect component ($\Delta\lambda_{temperature}$) is related to the change in index of refraction [12]:

$$\Delta\lambda_{temperature} = \lambda_{CW}\left(\alpha_f + \frac{1}{n_0}\frac{dn_0}{dT}\right)\left(T - T_0\right) \tag{6}$$

where $\lambda_{CW}$ is the Bragg center wavelength of the FBG sensor (1543.30 nm for the embedded FBG sensor, 1541.04 nm for the free-floating FBG sensor), $\alpha_f$ is the coefficient of thermal expansion (CTE) of the fiber (i.e. silica), $n_0$ is the index of refraction, $dn_0/dT$ is the thermo-optic coefficient, $T_0$ is defined as the temperature at the first measurement of the Bragg wavelength, $\lambda_0$, during calibration and $T$ is the temperature corresponding to any of the Bragg wavelength measurements.

The strain component ($\Delta\lambda_{strain}$) is given by:

$$\Delta\lambda_{strain} = \lambda_{CW}\left(1 - p_e\right)\left(\varepsilon - \alpha_f\left(T - T_0\right)\right) \tag{7}$$

Due to the physical elongation of the sensor as well as the change in refractive index due to photoelastic effects [12, 18], where $\varepsilon$ is the mechanical strain and $p_e$ is the photoelastic coefficient given by:

$$p_e = \left(\frac{n_0^2}{2}\right)\left[p_{12} - \nu\left(p_{11} + p_{12}\right)\right] \tag{8}$$

where $\nu$ is the Poisson's ratio of the fiber (i.e. silica) and $p_{11}$ and $p_{12}$ are Pockel's coefficients. Since these constants were not supplied by O/E Land Inc., typical values were selected for theoretical calculations [17, 51-54], as seen in Table 1.

Table 1. Optical fiber constants used in theoretical calculations

| | |
|---|---|
| $\alpha_s$, coefficient of thermal expansion of substrate (/°C) | $13.1 \times 10^{-6}$ |
| $\alpha_f$, coefficient of thermal expansion of fiber (/°C) | $0.55 \times 10^{-6}$ |
| $n_0$, index of refraction | 1.46 |
| $dn_0/dT$, thermo-optic coefficient (/°C) | $11 \times 10^{-6}$ |
| $\nu$, Poisson's ratio | 0.2 |
| $p_{11}$, Pockel's coefficient | 0.113 |
| $p_{12}$, Pockel's coefficient | 0.252 |

The mechanical strain can be calculated two different ways. The strain of the fiber surface is equivalent to the applied strain from the substrate in case of good contact and can be approximated by the following simple "CTE" equation:

$$\varepsilon = \alpha_s\left(T - T_0\right) \tag{9}$$

where $\alpha_s$ is the coefficient of thermal expansion of the substrate. Alternatively, the mechanical strain can be calculated via the analysis of a bimetallic beam. When a beam made up of two strips of materials of different elastic moduli and of different coefficients of thermal expansion is subject to a uniform temperature change it will bend [55, 56]. Its curvature and deflection, as well as the mechanical strain in the axial direction of either of the two strips, can be calculated. It has been shown that the curvature of a bimetallic beam is not too sensitive to differences in elastic moduli but is rather sensitive to the differences in the coefficients of thermal expansion [56]. Using this assumption it can be shown that the mechanical strain in the axial direction in the top strip can be calculated using the following "beam" equation:

$$\varepsilon = \alpha_{top}\left(T - T_0\right) + \frac{1}{4}\frac{\left(\alpha_{bottom} - \alpha_{top}\right)}{\left(1 + \frac{E_{top}}{E_{bottom}}\right)}\left(T - T_0\right) - \frac{3}{2h}\left(\alpha_{bottom} - \alpha_{top}\right)\left(y - \frac{h}{4}\right)\left(T - T_0\right) \qquad (10)$$

where $y$ is measured from the bottom of the bottom strip, $h$ is the total thickness of both strips, $\alpha_{top}$ is the coefficient of thermal expansion (CTE) of the top strip, $\alpha_{bottom}$ is the coefficient of thermal expansion (CTE) of the bottom strip, $E_{top}$ is the elastic modulus of the top strip, and $E_{bottom}$ is the elastic modulus of the bottom strip. In our case the top strip is nickel and the bottom strip is copper. This analysis can be applied to calculate the mechanical strain in the nickel coating layer of our nickel plated copper substrate near the embedded FBG sensor. The effects of mechanical strain *not* in the axial direction have been ignored.

In order to test the accuracy of the thermal response, the embedded FBG sensor and a free-floating FBG sensor were heated using a heat gun (the embedded FBG sensor was also cooled in an ice cube test). Temperatures were recorded from the FBG sensors using an O/E Land interrogator and software as well as a Type K thermocouple silver pasted to the surface of the nickel above the embedded FBG sensor. For the embedded FBG sensor, temperature measurements were recorded as the nickel plated copper substrate was heated *and* as it was cooling back to room temperature. The temperature measured by the thermocouple is plotted against the wavelength signal of the FBG sensors in Figure 22. The two FBG sensors exhibit different sensitivities, or slopes. Computing the slopes of the two sets of experimental points gives the following measured sensitivities: 0.0294 nm/°C for the sensitivity of the nickel embedded FBG sensor with a Bragg wavelength of 1543.30 nm and 0.0122 nm/°C for the free-floating FBG sensor with a Bragg wavelength of 1541.04 nm. The nickel coating increases the sensitivity of the FBG sensor by more than twice due to its high coefficient of thermal expansion that imposes significant strain, stretching the fiber more as temperature increases.

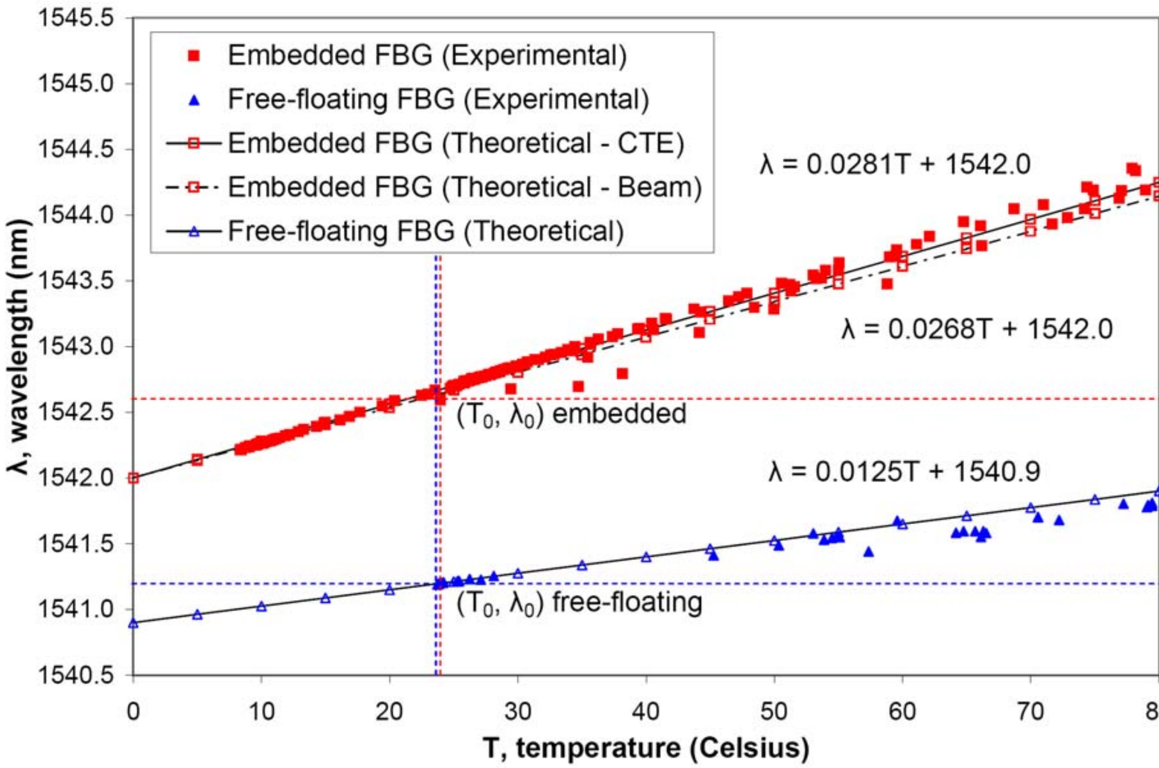


Figure 22. Thermal response of embedded and free-floating FBG sensors (intersection of dashed lines indicates start of experiment/calibration point)

Notice that several temperature measurements near the calibration point corresponding to the first heating of the embedded FBG sensor do not follow the theoretical prediction. This was not observed as the FBG sensor and assembly was allowed to cool back to room temperature, or during subsequent cycles. It is hypothesized that the polyimide coating allowed the cladding and core to "slip" within the coating during the first 10 or 20°C increase from room temperature during the first heating. For all subsequent heating and cooling cycles, it appears that a strong bond developed between the fiber and the substrate.

The theoretical sensitivity for the free-floating FBG sensor was calculated as 0.0125 nm/°C using Eqn. 5 with mechanical strain calculated using Eqn. 9 with $\alpha_f$ substituted for $\alpha_s$. This means that no mechanical force acts upon the free-floating FBG sensor. This calculation shows that the experimental sensitivity is 2.1% off from the theoretical sensitivity for the free-floating FBG sensor. The theoretical sensitivity for the embedded FBG sensor was calculated as 0.0281 nm/°C using Eqn. 9 to compute the mechanical strain (CTE method), shown plotted on the above figure. The alternative method of calculating mechanical strain using Eqn. 10 (beam method), produces a theoretical sensitivity for the embedded FBG sensor of 0.0268 nm/°C, shown plotted on the above figure. Both methods of predicting the mechanical strain yield theoretical sensitivities approximately 5% off the experimental sensitivity. When using Eqn. 10, this error is most likely due to the fact that the temperature change applied during testing is most likely *not* uniform. It is possible to predict the temperature measured by the FBG sensor by using the following equation:

$$T = \frac{1}{m}\left(\lambda - \lambda_0\right) + T_0 \qquad (11)$$

where $m$ is the sensitivity (either theoretical or experimental), $\lambda$ is the Bragg wavelength, and $\lambda_0$ and $T_0$ are the Bragg wavelength and temperature measured at calibration, respectively.

To avoid calibration, the free-floating FBG sensor gives correct absolute temperature predictions for the reference temperature, $T_0'$, of 10°C, (which is presumably the actual ambient temperature that corresponds with the center wavelength, $\lambda_{CW}$, from the manufacturer). For the embedded fiber, the reference temperature $T_0'$ appears to be 48°C. This is presumably higher than the actual reference temperature from manufacturing. This is likely due to mechanical strain due to compressive residual stress arising during the electro-plating process. Assuming the same actual reference temperature of 10°C, and an elastic modulus of 207 GPa for the nickel coating layer, this corresponds to a residual stress, $\sigma = -E\alpha_s\left(T - T_0'\right)$, of -103 MPa.

In order to predict the best temperature reading, the temperature and strain effects must be decoupled. The best way to decouple the temperature and strain effects is to insert the FBG sensor into a hollow stainless steel tube that allows it to freely expand as it is heated prior to being nickel plated to embed it in the coating layer. Because the sensor can freely expand, the effect of strain on the signal output of the sensor is eliminated. Therefore, the wavelength signal is linearly related to the temperature of the host material according to Eqn. 6 only. No extensive calibration of the FBG sensor signal would be necessary as the fiber would expand and contract like a free-floating FBG sensor. This method has the added benefit of solving the handling issues associated with placing the FBG sensor on the mold face prior to plating. Since a 300 μm to 400 μm thick nickel coating layer is used on copper continuous casting molds the stainless steel tube must be less than 400 µm, but preferably less than 300 µm. The size of the tube also depends on the diameter of the FBG sensor. An easy to handle, polyimide coated sensor has a diameter of 155 µm while a bare fiber, which requires very carefully handling, is approximately 125 µm in diameter.

Two different sizes of 316 stainless steel tubes were purchased from McMaster-Carr. The larger of the two tubes (OD 330 µm, ID 178 µm) is capable of housing a coated sensor while the smaller of the two tubes is capable of housing a bare fiber (OD 254 µm, ID 127 µm). It might become necessary to use a bare fiber with the small stainless steel tube if the nickel coating layer is less than 330 µm. Sections of each size tube were nickel plated onto a copper substrate with the ends of the tubes left open, following a similar procedure as outlined above. The tubes were successfully embedded in the nickel coating layer and the surface of the nickel was machined flat by hand to improve appearance (Figure 23). To prove the feasibility of this sensor application, a polyimide coated FBG sensor was inserted into the appropriate stainless steel tube by placing the copper substrate with embedded stainless steel tubes under an optical microscope (Figure 24). In this matter it would be possible to equip a mold with numerous FBG sensors and could even allow replacement of damaged FBG sensors without removing the nickel coating layer.

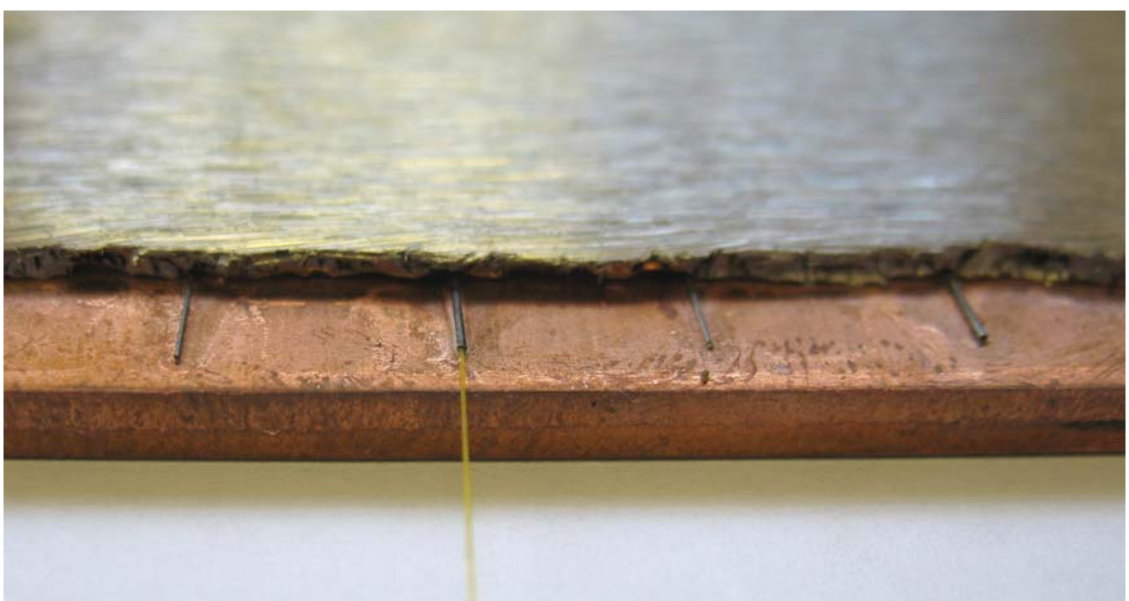

Figure 23. Stainless steel tubes embedded in nickel coating layer

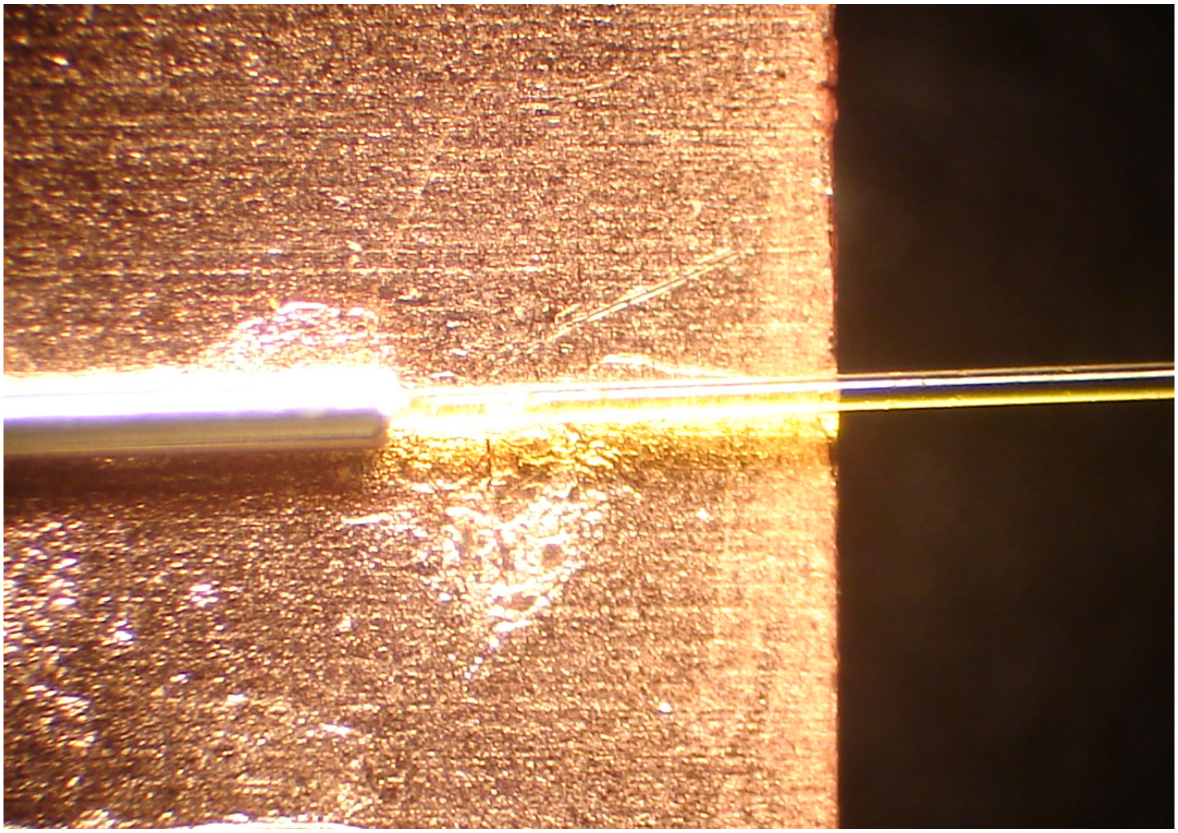

Figure 24. Polyimide coated FBG sensor inserted into a stainless steel tube

## 5. Air Gap Effect on Heat Transfer in the Continuous Casting Mold

An incorrect attachment procedure can result in an air gap between the conductive sensor strip and the copper mold. In service, such an air gap can decrease heat transfer and cause a localized high temperature region near the sensor. Such a local temperature increase at the mold hot face can cause defects in the steel or even cause coating layer failure [28, 29]. A computational model has been developed and applied to quantify this behavior.

### *5.1 Model Formulation*

A two dimensional finite element heat transfer and thermal stress model has been developed to understand the thermal and mechanical behavior of coating layers with an air gap present. The temperature distribution in the coating layer and mold can be obtained by modeling 2-D steady-state heat conduction in the domain with the boundary conditions as shown in Figure 25. The same domain and mesh are used to conduct a thermal stress analysis based on the calculated temperature profiles.

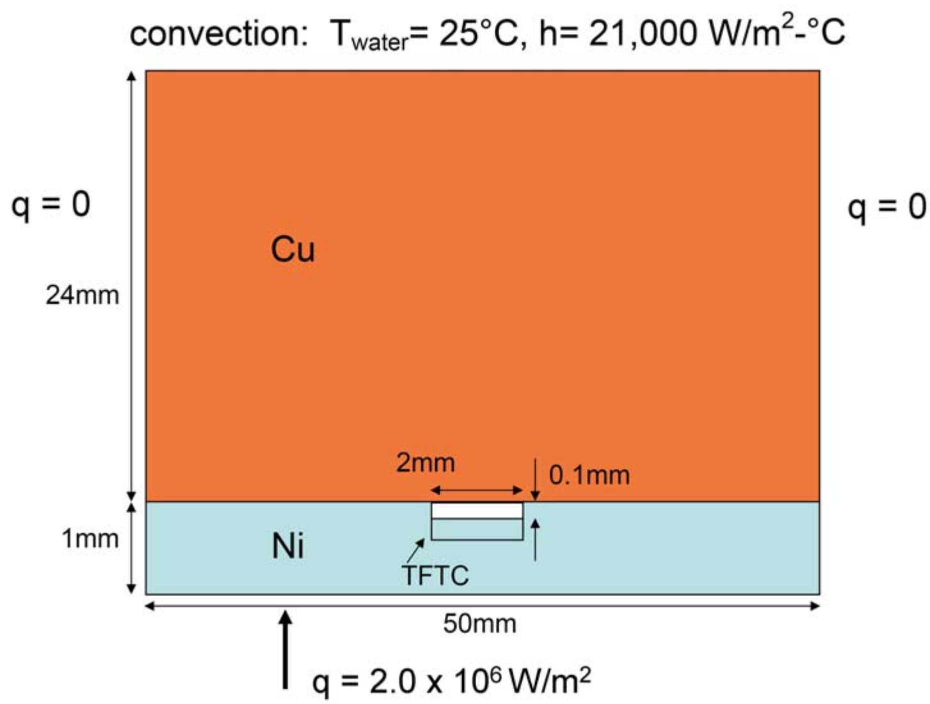


Figure 25. Two dimensional domain for heat transfer and thermal stress analysis

The hot face (bottom on above figure) was subjected to a fixed heat flux of 2.0 x $10^6$ W/$m^2$ to represent the interface between the solidifying steel shell and the surface of the mold. Due to symmetry, an insulated boundary condition was applied on the two vertical ends. On the top surface, a heat convection boundary condition with heat transfer coefficient of 21,000 W/ $m^2$-°C and ambient temperature of 25°C was employed. Density, thermal conductivity, specific heat, elastic modulus, Poisson's ratio, and coefficients of thermal expansion for copper and nickel are listed in Table 2. They are considered independent of temperature in the model. The following energy balance equation for this 2-D problem was solved:

$$k\nabla^2 T = 0 \tag{12}$$

where $k$ is the thermal conductivity. For the thermal stress model the domain was allowed to freely expand. The stress state was generalized plane strain. The temperature solution is one-dimensional far from the air gap region. This was used to validate the model by comparing the predictions there to the following analytical solutions derived using the composite wall method [45]:

$$T_{hotface} = q\left[\left(\frac{t_{Ni}}{k_{Ni}}\right) + \left(\frac{t_{Cu}}{k_{Cu}}\right) + \left(\frac{1}{h}\right)\right] + T_{water} \tag{13}$$

$$T_{Ni} = T_{hotface} - q\left[\left(\frac{x_i}{k_{Ni}}\right)\right] \tag{14}$$

$$T_{interface} = T_{hotface} - q\left[\left(\frac{t_{Ni}}{k_{Ni}}\right)\right] \tag{15}$$

$$T_{Cu} = T_{hotface} - q\left[\left(\frac{t_{Ni}}{k_{Ni}}\right) + \left(\frac{x - t_{Ni}}{k_{Cu}}\right)\right] \tag{16}$$

where $x$ is the distance from the hotface (mm).

Table 2. Materials properties of copper and nickel used in the heat transfer and thermal stress analysis

| | Cu | Ni |
|---|---|---|
| ρ, density ($kg/m^3$) | 8960 | 8890 |
| k, thermal conductivity (W/m-°C) | 350 | 70 |
| $C_p$, specific heat (J/kg-°C) | 380 | 456 |
| E, elastic modulus (GPa) | 110 | 207 |
| ν, Poisson's ratio | 0.343 | 0.31 |
| α, coefficient of thermal expansion (/°C) | $17.7 \times 10^{-6}$ | $13.1 \times 10^{-6}$ |

### *5.2 Solution Methodology*

The commercial finite element package ANSYS was used to perform both the thermal and stress analysis. The standard 4-node 2-D heat transfer element PLANE55 was used for heat transfer analysis and the 4-node, 2-D plane strain stress element PLANE42 was used for the stress analysis. Both elements are quadratic, four-node types. A sequentially coupled thermal stress analysis was adopted. First, the thermal problem was defined and solved with the heat transfer model solely. Second, element types were switched and additional material properties (i.e. elastic modulus, Poisson's ratio, and thermal expansion coefficients) and structural boundary conditions were specified. Then, the temperature field was read into the stress model at nodes as a predefined thermal load and the stress problem was solved.

A parametric study of the size of the air gap was performed to determine the effect on heat transfer. In the original air gap case, the air gap was 2 mm wide and 0.1 mm thick. In the thicker air gap case the thickness of the air gap was increased to 0.2 mm and in the wider air gap case the width of the air gap was increased to 4 mm. Temperatures were recorded for various distances away from the hot face at the gap centerline (the exact center of the domain), the gap edge (the end of the gap), and at a distance considerably far away from the gap.

*5.3 Results*

The temperature contour plot for the original air gap case is shown in Figure 26. Far from the air gap, the hot face, nickel coating layer (0.496 mm from the hot face), interface, and copper (2.4578 mm from the hot face) temperatures are 286°C, 272°C, 257°C, and 249°C, respectively, which matches the analytical, one-dimensional heat transfer solutions in Eqns. 13-16. For the original geometry case the hot face temperature at the gap centerline was 314°C. For the wider air gap case the hot face temperature was 379°C while for the thicker air gap case the hot face temperature was 319°C. As seen in Figure 27, a wider gap makes it much more difficult for heat to conduct around the gap. Increasing gap thickness naturally has a similar effect, but is not as important: doubling the width of the air gap increases the hot face temperature by 65°C, an increase of 21%, while doubling the thickness of the air gap increases the hot face temperature by only 5°C, an increase of less than 2%.

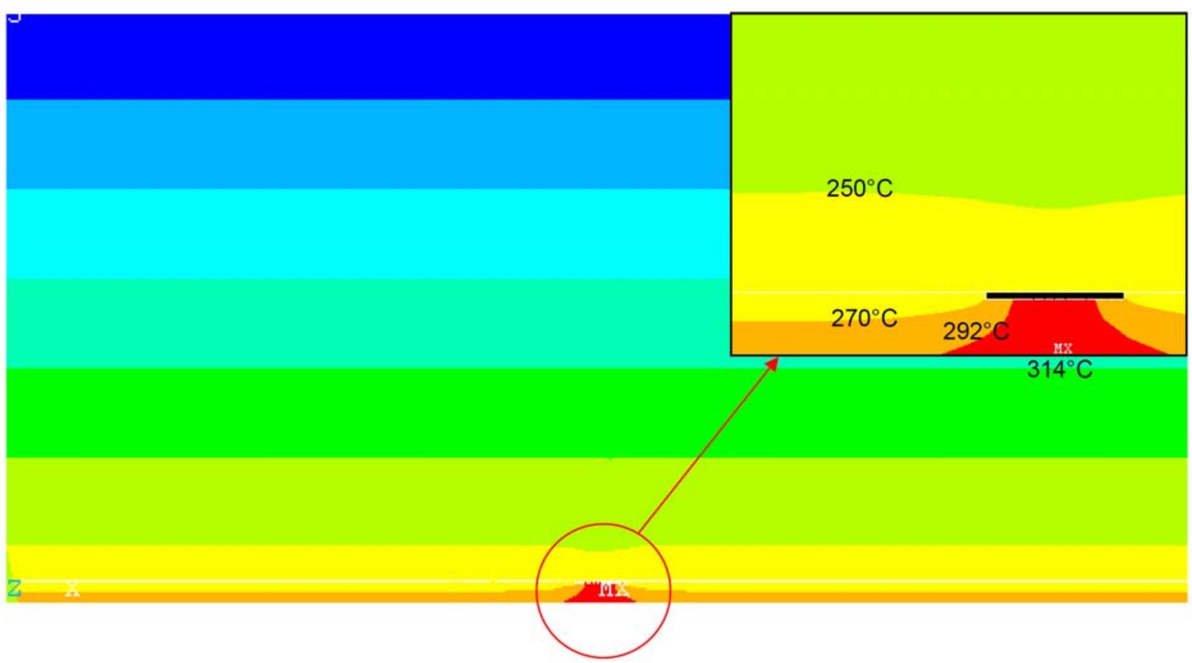


Figure 26. Temperature contour plot for original air gap case with temperatures near the air gap region

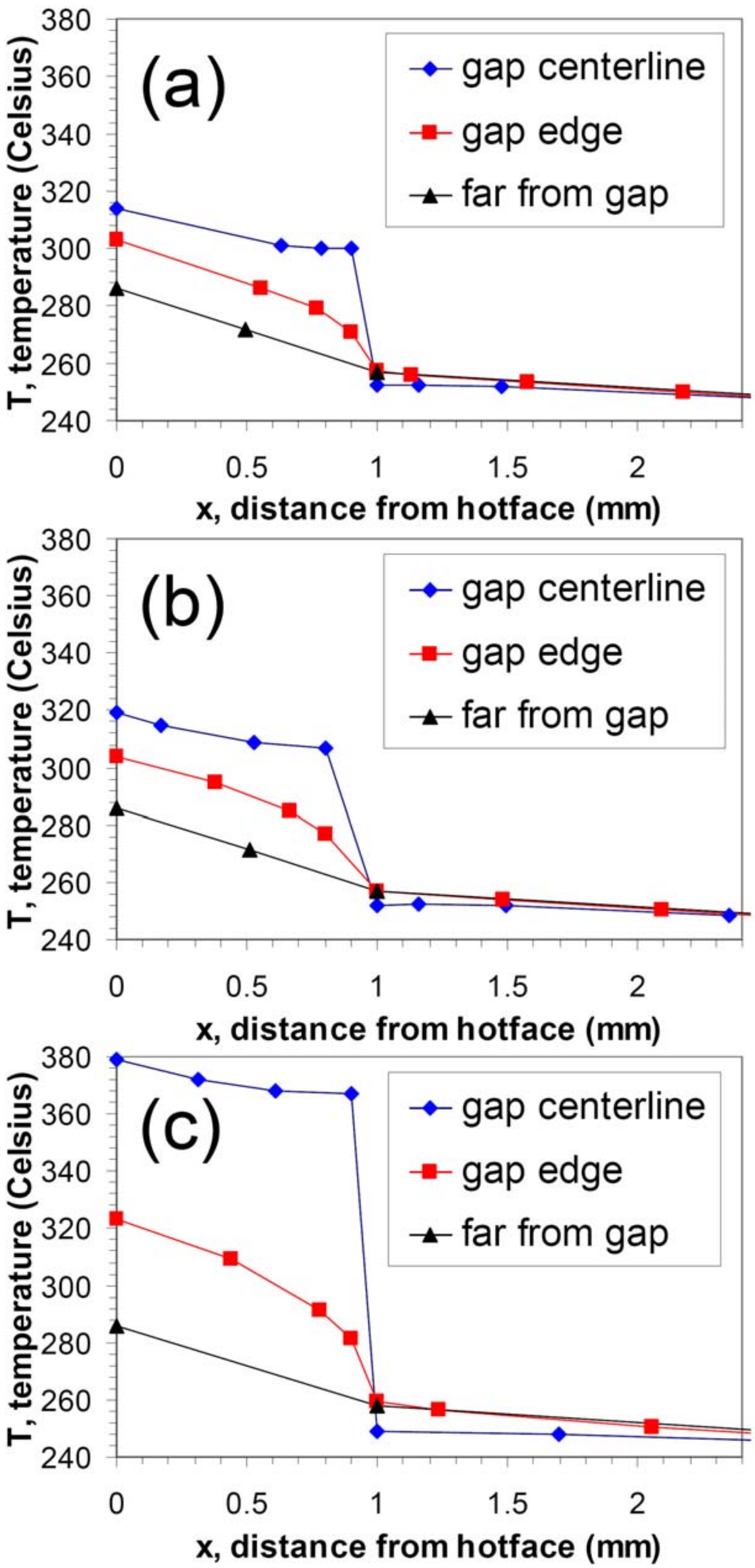


Figure 27. Results of parametric study of heat transfer around an air gap for (a) original geometry, (b) thicker gap, and (c) wider gap

The thermal stress contour plot for the original air gap case is shown in **Figure 28**. The thermal stress analysis indicated that, as a result of the calculated temperature profiles, the copper goes into compression while the nickel coating layer goes into tension, for a domain both with and without an air gap. In other words, the copper attempts to expand more than the nickel layer. The corner effects are far enough away not to affect the air gap region. Without an air gap, the maximum stress in the copper was 67.8 MPa (compression) and the maximum stress in the nickel coating layer was 185 MPa (tension). With a 2 mm wide and 0.1 mm thick air gap, the maximum stress in the copper was 67.8 MPa (compression) and the maximum stress in the nickel coating layer was 276 MPa (tension) at the corner of the air gap, a 50% increase in the maximum stress in the nickel coating layer. However, the stress in the copper directly above the air gap region was 30 MPa (compression) and the stress in the nickel coating layer directly below the air gap region was 200 MPa (tension), an increase of 8% compared to the thermal stress analysis without an air gap. In both cases the yield stress of the nickel coating layer ($\sigma_y$ = 148 MPa) was exceeded [57], while the stress in the copper is too low to make the copper yield [58]. Therefore, the nickel layer might locally yield, debond, or spall off in patches.

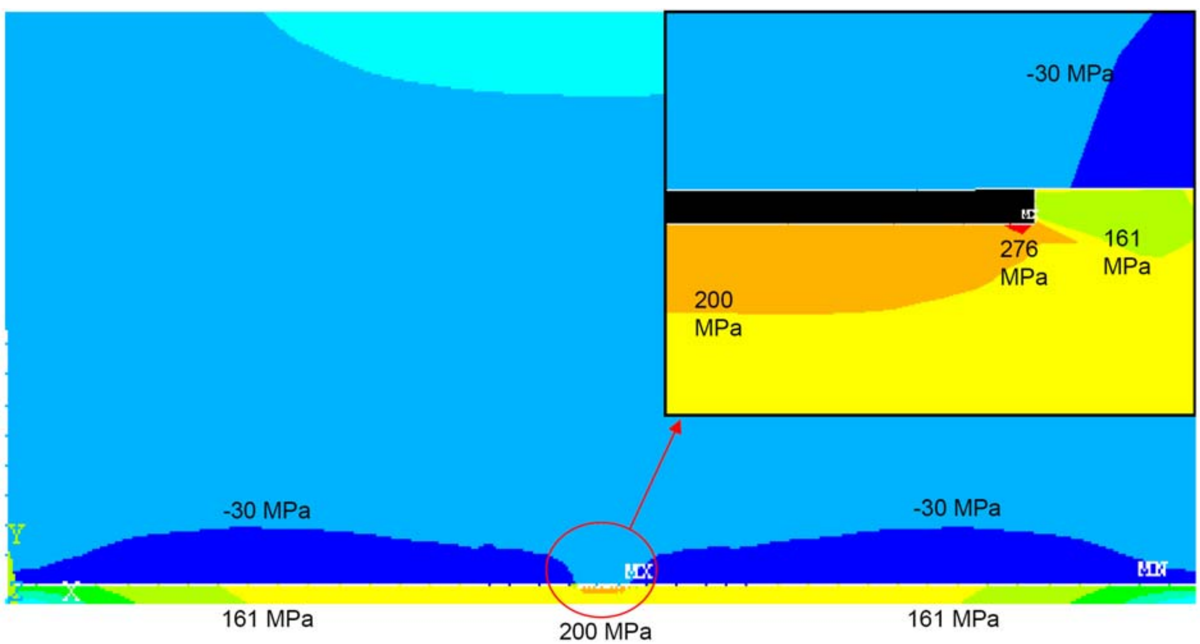


Figure 28. Thermal stress contour plot for original air gap case with stresses near the air gap region

## 6. Conclusions

Microfabricated thin-film thermocouples (TFTCs) and Fiber Bragg Grating (FBG) sensors can be embedded in the nickel coating layer of a copper mold of a continuous caster to measure temperature and heat flux. Embedded sensors have the advantage of real-time monitoring at critical locations as well as immunity to electromagnetic interference and resistance to hostile environments, but cannot be commercial successful without a robust attachment method. This thesis highlights the design and installation process for a new type of mold sensor for use in the commercial continuous casting of steel. The work outlined in this thesis has lead to the following conclusions:

- A novel TFTC capable of measuring temperature and heat flux has been designed for use in continuous casting molds.
- It has been demonstrated that wireless thermocouple technology can be used to transmit temperature data to a receiver in the caster pulpit.
- It has been shown that if a rectangular shaped sensor is plated over without first being affixed to the mold an air gap will result.
- A wider air gap makes it more difficult for heat to conduct around the gap, increasing the temperature at the hot face: doubling the width of the air gap increases the hot face temperature by 65°C, an increase of ~20%, while doubling the thickness of the air gap increases the hot face temperature by only 5°C, an increase of less than 2%.
- The thermal stress analysis with an air gap indicated that, as a result of the calculated temperature profiles, the copper goes into compression ($\sigma^{max}$ = 67.8 MPa) while the nickel coating layer goes into tension ($\sigma^{max}$ = 276 MPa); therefore, the nickel layer might yield, debond, or spall off in patches.
- The thermal stress analysis determined that the presence of an air gap 2 mm wide and 0.1 mm thick causes an ~10-50% increase in the stress in the nickel coating layer, compared to a nickel coating layer without an air gap.
- Ultrasonic welding has not been found to be an acceptable solution to the sensor attachment problem due to the unavoidable cracking and distortion that occurs near, around, or on top of sensors during welding.

- A robust, although time consuming, method using conductive silver paste was developed to embed TFTCs in a coating layer, after numerous plating studies.
- The signal output by FBG sensors embedded in a nickel coating layer has been investigated and can be predicted with simple equations.
- It is hypothesized that the polyimide coating on the embedded FBG sensor allowed the cladding and core to "slip" within the coating during the first 10 or 20°C increase from room temperature during the first heating.
- In order to ensure a reliable, accurate temperature reading, a FBG sensor should be inserted into a stainless steel tube that allows it to freely expand prior to being nickel plated to embed it in the coating layer.

## 7. Future Work

Although a novel TFTC well suited for use in continuous casting molds has been designed, it has not yet been fabricated. Work continues at the University of Wisconsin at Madison to design new TFTC sensors. Concurrently, research at the University of Illinois at Urbana-Champaign continues to explore the implementation of FBG sensors applied to continuous casting molds. Due to the complexity associated with interpreting the signal output from an embedded FBG sensor, it is recommended that the sensor be installed in a stainless steel tube. The stainless steel tube can be embedded in the coating layer prior to the insertion of the FBG sensor, or after, thus eliminating the handling issues encountered during plating at a commercial facility. Using this technique it is possible to outfit a mold face with FBG sensors that will measure temperature solely. The next step will be to conduct an industrial trial with an instrumented mold.

Another task will be to interpret the signals from the embedded sensor. One benefit will be to discover new insights into meniscus phenomena and defect formation, which arise at the meniscus. The "budget" interrogator system currently utilized will have to be replaced with a more advanced system with several channels and a much higher data rate. In the meantime, work to improve understanding of meniscus phenomena is proceeding at the University of Illinois at Urbana-Champaign using computational models, metallography, and microscope analysis of plant samples, previous laboratory experiments, and conventional temperature measurements.

Eventually, sensor signals obtained online at the commercial caster will be correlated with defects in cast steel found by evaluation of the cast product. This work will have the most commercial impact. Efforts will be made to identify characteristic signals or “signatures” of the formation of particular individual defects. This will advance the technology towards the ultimate commercialization of an “expert mold”. Improving this important process even slightly has a huge potential impact in energy savings, yield savings, steel quality, and efficiency improvement, because this particular process is used to produce several hundred million tons of steel every year.

## Appendix A: Basic Operations Manual for MicroStrain® TC-Link® System

This manual, or guide, is provided as a brief overview to the setup and operation of the MicroStrain® TC-Link® system. It is intended to be a supplement to the comprehensive MicroStrain® manual provided by MicroStrain® on CD-ROM.

I. Required Equipment

1. MicroStrain® USB Base Station (receiver)
2. TC-Link® node (transmitter)
3. Type K thermocouple
3. TC-Link® node AC adapter to charge the node, if necessary
4. Computer with USB support
5. MicroStrain® software (on provided CD-ROM)

II. Setup

1. Insert the MicroStrain® CD-ROM into the optical drive of the computer.
2. Follow all onscreen instructions to install the MicroStrain® software on the computer.

III. Operation (Temperature Measurement)

1. Connect the USB Base Station into a USB port on the computer. A blue light on the USB Base Station should illuminate.
2. Connect the Type K thermocouple to the TC-Link® node. Remember that the Type K thermocouple can only be connected in one way, as one pin of the thermocouple is larger than the other. Do not force it!
3. Turn on the node by flipping the switch on the side of the node. If the green light on the node is not blinking, try charging the node.
4. Open/run the MicroStrain® software.
5. The software will prompt you to select the communication port (COMx, the value of x depending on your computer). You can see a list of the operational communication ports by opening 'Device Manager.' One way to do this is to right

click 'My Computer,' click 'Properties,' click 'Hardware,' and click 'Device Manager.' If you are unsure which communication port is being used by MicroStrain®, you can unplug the USB Base Station. The communication port that disappears is the correct one.

6. Once a communication port is selected, the node Real-Time Panel will appear. Both Real-Time Graph and Real-Time Log provide a constantly updated temperature plot or log, respectively. The units of temperature can be changed by clicking the slider on the right side of the Real-Time Graph.

7. When all measurements are completed, click the 'Save to CSV' button under the 'Real-Time Log' tab to save the temperature measurements in an easy to use comma separated value file. DO NOT CLICK THE 'STOP' BUTTON UNDER THE 'REAL-TIME GRAPH' TAB BEFORE YOU SAVE YOUR MEASUREMENTS AS THEY WILL BE ERASED!

8. Now click the 'STOP' button and close all windows. Unplug the USB Base Station and power off the node.

## Appendix B: Basic Operations Manual for OEFSS-200 Interrogator System

This manual, or guide, is provided as a brief overview to the setup and operation of the O/E Land Inc. OEFSS-200 FBG Sensing System / Tunable Laser interrogator. It is intended to be a supplement to the O/E Land User Guide provided by O/E Land Inc. on CD-ROM.

I. Required Equipment

1. O/E Land Inc. OEFSS-200 FBG Sensing System / Tunable Laser interrogator
2. FBG sensor (transmission-type) with center wavelength within bandwidth of interrogator
3. Another temperature measurement device (i.e. thermometer, thermocouple, etc.)
3. Computer with USB support
4. USB cable (type-A to type-B)
5. Power cable
6. O/E Land software (on provided CD-ROM)

II. Hardware Setup

1. Install driver for OEFSS-200 (first time operation only).
   - A. Turn on OEFSS-200 via power switch on front panel. Do not turn on the laser at this time.
   - B. Connect the USB cable from OEFSS-200 to the computer.
   - C. 'Found New Hardware' wizard should appear. Make sure 'Yes, this time' is selected and click 'Next.'
   - D. Browse the CD-ROM provided and locate the file MCHPCDC in the folder 'win2k_winxp' and click 'Next.'
   - E. Select 'Continue Anyway.'
   - F. Click 'Finish' to complete the wizard.
2. Connect OEFSS-200 with the computer.
   - A. Turn on OEFFS-200 via power switch on front panel, if it currently off.
   - B. The USB connection of OEFSS-200 operates as a communication (COM) port.

C. Open 'Device Manager.' One way to do this is to right click 'My Computer,' click 'Properties,' click 'Hardware,' and click 'Device Manager.'

D. Click 'Ports.' An additional communication port (COMx, the value of x depending on your computer) should appear.

E. If you are unsure if OEFSS-200 is communicating with the computer, remove the USB cable from either the computer or OEFSS-200. The communication port should disappear.

III. Software Setup

1. Install the OEFSS-200 Utility software provided by O/E Land Inc. on CD-ROM.

   A. Find the folder entitled 'Utility Software' on the CD-ROM. Double click the setup.exe file and follow the onscreen instructions.

2. Open/run the O/E Land software.

IV. Operation (Temperature Measurement)

1. Make sure the OEFSS-200 is powered on and connected to the computer and that it is communicating with computer.

2. Plug one end (it does not matter which end) of the transmission-type FBG sensor into the 'Output' port on the front panel of the OEFSS-200 and plug the other end into the 'Input/Adjust' port. Do not overtighten the connectors.

3. Turn the laser on by flipping the switch on the front panel of the OEFSS-200.

4. Wait at least 5 seconds for the laser to warm up.

5. Click the 'Execute' button. It will take the laser more than a minute to find the center wavelength of the FBG sensor. The green bar under the 'Execute' button shows you the progress of the sweep. An image of the spectrum waveform will appear on the top half of the screen.

   (Note: A series of vertical lines indicate there is a problem. Reconnect the FBG sensor, clean the connectors of the sensor and/or the connectors of the OEFSS-200 if dirty, and make sure that the FBG sensor has a center wavelength within the bandwidth of the OEFSS-200.)

6. When the sweep is finished, a number will appear under 'Sensor CW' under the 'Wavelength' tab on the bottom half of the screen. This is the center wavelength (in nm) of the FBG sensor at room temperature.

7. Click the 'Temperature' tab on the bottom half of the screen. Type in the 'Sensor CW' that was just generated and the temperature (in degrees Celsius) at which the sweep was executed.

8. Perform another sweep by clicking the 'Execute' button. After a minute or so of sweeping, the number under 'Sensor CW' will regenerate (if the temperature is constant, the number should be very similar to the previous).

9. Click the 'Temperature' tab. A temperature should appear under 'temperature.' This number will regenerate each time a sweep is performed.

> (Note: It is best to record the center wavelength and temperature for each sweep in a separate location, either digitally or physically. The system provided to record this information is poorly designed.)

10. For additional temperature measurements, continue to execute sweeps of the laser. To finish measurements, click the 'Quit' button next to the 'Execute' button and close all windows. Turn the OEFSS-200 off and unplug it.

## References


1. Badri, A.B. and A.W. Cramb. *Thermocouples - what are they measuring?* in *59th Electric Furnace Conference and 19th Process Technology Conference*. 2001. Phoenix, AZ.
2. Grant, H.P. and J.S. Przybyseweski, *Thin Film Temperature Sensors.* J. Eng. Power, 1977. **99**(497).
3. Kinard, J.R., D.X. Huang, and D.B. Novotny, *Performance of Multi-layer Thin-Film Multijunction Thermal Convertors.* IEEE Trans. Instrum. Meas., 1995. **44**: p. 383-386.
4. Kreider, K.G. and F. DiMeo, *Platinum/palladium Thin-Film Thermocouples for Temperature Measurements on Silicon Wafers.* Sens. Actuators A, 1998. **69**: p. 46-52.
5. Choi, H., et al., *Microfabrication and Characterization of Metal-Embedded Thin-Film Thermomechanical Microsensors for Applications in Hostile Manufacturing Environments.* Journal of Microelectromechanical Systems, 2006. **15**(2): p. 322-329.
6. Zhang, X., et al., *Design, Fabrication, and Characterization of Metal Embedded Thin-Film Thermocouples with Various Film Thicknesses and Junction Sizes.* J. Micromech. Microeng., 2006. **16**: p. 900-905.
7. Datta, A., H. Choi, and X. Li, *Batch Fabrication and Characterization of Micro-Thin-Flim Thermocouples Embedded in Metal.* Journal of the Electrochemical Society, 2006. **153**(5): p. H89-H93.
8. Hill, K.O., et al., *Photosensitivity in optical waveguides: Application to reflection filter fabrication.* Applied Physics Letters, 1978. **32**(10): p. 647.
9. Butter, C.D. and G.B. Hocker, *Fiber Optics Strain Gauge.* Applied Optics, 1978. **17**(18): p. 2867-2869.
10. Meltz, G., W.W. Morey, and W.H. Glenn, *Formation of Bragg gratings in optical fibres by transverse holographic method.* Opt. Lett., 1989. **14**(15): p. 823.
11. Udd, E., *Fiber Optic Smart Structures*. 1995, New York: Wiley (Interscience).
12. Li, X. and F. Prinz, *Metal Embedded Fiber Bragg Grating Sensors in Layered Manufacturing.* Journal of Manufacturing Science and Engineering, 2003. **125**: p. 1-9.
13. Trpkovski, S., et al., *Dual temperature and strain sensor using a combined fiber Bragg grating and fluorescence intensity ratio technique in Er3+ -doped fiber.* Review of Scientific Instruments, 2003. **74**(5): p. 2880-2885.
14. Baldini, S.E., D.J. Tubbs, and W.A. Stange, *Embedding Fiber Optic Sensors in Titanium Matrix Composites.* Fiber Optic Smart Structurs and Skins III, SPIE, 1990. **1370**: p. 162.
15. Taylor, H.F. and C.E. Lee, *Sensing Applications of Fiber Fabry-Perot Interferometers Embedded in Composites and in Metals.* Experiments in Smart Materials and Structures, ASME, AMD, 1993. **181**: p. 47.
16. Lee, C.E., et al., *Method for Embedding Optical Fibers and Optical Fiber Sensors in Metal Parts and Structures.* Fiber Optic Smart Structurs and Skins IV, SPIE, 1991. **1588**: p. 110.
17. Lee, C.E., et al., *Metal-embedded Fiber-optic Fabry-Perot Sensors.* Optics Letters, 1991. **16**(24): p. 1990-1992.

18. Yu, X., et al., *Strain Measurement of Steel Structure Using a Novel FBG Sensor Packaged by Titanium Alloy Slice.* Proc. of SPIE, 2005. **6019**.
19. Eroglu, M., T.I. Khan, and N. Orhan, *Diffusion bonding between Ti-6Al-4V alloy and microduplex stainless steel with copper interlayer.* Materials Science and Technology, 2002. **18**.
20. Batra, I.S., et al., *Diffusion bonding of a Cu-Cr-Zn alloy to stainless steel and tungsten using nickel as an interlayer.* Materials Science and Engineering, 2004. **A369**: p. 119-123.
21. Esposito, L., et al., *Solid state bonding of Al2O3 with Cu, Ni, and Fe: characteristics and properties.* Journal of Materials Science, 1998. **33**: p. 1827-1836.
22. Coughlan, F.M. and H.J. Lewis, *The development of a tri-material system and appropriate bonding parameters for the thermal bonding of flat leads.* Journal of Materials Processing Technology, 2004. **153-154**: p. 240-246.
23. Peterson, J.M., H.L. McKaig, and C.F. DePrisco, *Ultrasonic Welding in Electronic Devices.* IRE National Convention, 1962: p. 3-12.
24. Antonevich, J., *Ultrasonic Welding Equipment.* IRE Transactions on Ultrasonic Engineering, 1960. **7**(1): p. 26-31.
25. Francis, S.A., *Techniques, Equipment, and Procedures for Production Welding of Electronics.* IEEE Transactions on Product Engineering and Production, 1963. **7**(1): p. 13-17.
26. Hayashi, K., et al., *New type of large-area a-Si module produced using a polymer encapsulation method.* IEEE First World Conference on Photovoltaic Energy Conversion, 1994. **1**: p. 535-538.
27. Krempl, P.W., et al., *Temperature sensors based on GaPO4.* Proceedings of the IEEE 2002 Ultrasonics Symposium, 2002. **1**: p. 949-952.
28. Teixeira, V., *Numerical analysis of the influence of coating porosity and substrate elastic properties on the residual stresses in high temperature graded coatings.* Surface and Coatings Technology, 2001. **146-147**: p. 79-84.
29. Amirhaghi, S., et al., *Diamond coatings on tungsten carbide and their erosive wear properties.* Surface and Coatings Technology, 2001. **135**: p. 126-138.
30. Schlesinger, M. and M. Paunovic, *Modern Electroplating*. 4th ed. 2000, New York: Wiley.
31. Jorne, J. and A.M. Tran, *Additive-free electroplating of copper in high-aspect-ratio trenches.* Proceedings of the IEEE 2001 International Interconnect Technology Conference, 2001: p. 27-29.
32. Chiu, S., et al., *Characterization of additive systems for damascene Cu electroplating by the superfilling profile monitor.* Journal of Vacuum Science and Technology B: Microelectrics and Nanometer Structures, 2000. **18**(6): p. 2835-2841.
33. Ibanez, A. and E. Fatas, *Mechanical and structural properties of electrodeposited copper and their relation with the electrodeposition parameters.* Surface and Coatings Technology, 2005. **191**: p. 7-16.
34. Tuck, J.R., et al., *Modelling of the hardness of electroplated nickel coatings on copper substrates.* Surface and Coatings Technology, 2000. **127**: p. 1-8.
35. Kessler, T. and R. Alkire, *A model for copper electroplating of multilayer printed wiring boards.* Journal of the Electrochemical Society: Electrochemical Science and Technology, 1976. **123**(7): p. 990-999.

36. Ritter, G., et al., *Two- and three-dimensional numerical modeling of copper electroplating for advanced ULSI metallization.* Solid State Electronics, 2000. **44**(5): p. 797-807.
37. Andricacos, P.C., et al., *Damascene copper electroplating for chip interconnections.* IBM Journal of Research and Development, 1998. **42**(5): p. 567-574.
38. Raub, E. and K. Muller, *Fundamentals of Metal Deposition*. 1967: Elsevier Publishing Company. 41-47.
39. Lyons, H.J., *Modern Electroplating*. 3rd ed, ed. F.A. Lowenheim. 1974, New York: John Wiley. 1-12.
40. Glasstone, S., *The Fundamentals of Electrochemistry and Electrodeposition*. 1960: Franklin Publishing Company. 17-25.
41. Campbell, J., *Castings*. 1991, Oxford: Butterworth-Heinemann Ltd.
42. Morthland, T.E., et al., *Optimal Riser Design for Metal Castings.* Metallurgical and Materials Transactions B, 1995. **26B**: p. 871-885.
43. Hausild, P., et al., *Ductile fracture of duplex stainless steels with casting defects.* International Journal of Pressure Vessels and Piping, 2001. **78**: p. 607-616.
44. Martin, L.C., J.D. Wrbanek, and G.C. Fralick, *Thin Film Sensors for Surface Measurements*. 2001, NASA. p. 1-5.
45. Incropera, F.P. and D.P. DeWitt, *Fundamentals of Heat and Mass Transfer*. Fifth ed. 2002: John Wiley & Sons, Inc. 88-93.
46. Bhatt, H., M. Zeller, and H.A. Will, *Novel Thin-Film Heat Flux Sensors*, in *NASP Conference*. 1992: Orlando, FL.
47. Will, H.A. and H. Bhatt, *Status of Thin Film Heat Flux Sensors.* NASA CP-3282, 1994: p. 127-132.
48. Sirkis, J.S. and A. Dasgupta, *What Do Embedded Optical Fibers Really Measure?*, in *1st European Conference on Smart Structures and Materials*. 1992, EOS/SPIE and IOP Publishing: Glasgow. p. 69-72.
49. Kollar, L.P. and R.J.V. Steenkiste, *Calculation of the Stresses and Strains in Embedded Fiber Optic Sensors.* Journal of Composite Materials, 1998. **32**(18): p. 1647-1679.
50. Steenkiste, R.J.V. and L.P. Kollar, *Effect of the Coating on the Stresses and Strains in an Embedded Fiber Optic Sensor.* Journal of Composite Materials, 1998. **32**(18): p. 1680-1711.
51. Dasgupta, A., J.S. Sirkis, and C. Liu, *The Importance of Coatings to Structurally Embedded Optical Fiber Sensors.* Advances in Instrumentation, Proceedings, 1990. **45**(4): p. 1673-1693.
52. Wagreich, R.B., et al., *Effects of Diametric Load of Fiber Bragg Gratings Fabricated in Low Bifringent Fiber.* Electron Lett., 1996. **26**(6): p. 1223-1224.
53. Kim, K.S., *A Model of Embedded Fiber Optic Fabry-Perot Temperature and Strain Sensors*. 1992, Stanford University.
54. Giallorenzi, T.G., et al., *Optical Fiber Sensor Technology.* IEEE Transactions on Microwave Theory and Techniques, 1982. **MTT-30**(4): p. 475.
55. Boley, B.A. and J.H. Weiner, *Theory of Thermal Stresses*. 1960, New York: Wiley. 429-432.
56. Timoshenko, S., *Bending and Buckling of Bimetallic Strips.* J. Optical Soc. of Am., 1925. **11**: p. 233.

57. Callister, W.D., *Materials Science and Engineering: An Introduction*. 5th ed. 2000: John Wiley & Sons, Inc.
58. Li, G. and B.G. Thomas, *Modeling Creep and Fatigue of Copper Alloys*, in *Continuous Casting Consortium*. 1999, University of Illinois at Urbana-Champaign. p. 30.